Supplementary Information for

Horizontally aligned carbon nanotube arrays: growth mechanism, controlled synthesis, characterization, properties and applications

Rufan Zhang[a†], Yingying Zhang[b], Fei Wei[a]*

a. Beijing Key Laboratory of Green Chemical Reaction Engineering and Technology, Department of Chemical Engineering, Tsinghua University, Beijing 100084, China. Email: wf-dce@tsinghua.edu.cn
b. Department of Chemistry and Center for Nano and Micro Mechanics, Tsinghua University, Beijing 100084, China
† Current address: Department of Materials Science and Engineering, Stanford University, Stanford, CA 94305, USA. Email: rfzhang@stanford.edu

Supplementary Text S1.

1. Mechanism for nucleation and growth of general CNTs

1.1 Nucleation and growth of CNTs

1.1.1 The nucleation process of CNTs

For the metal nanoparticles catalyzed CNT growth, the nucleation is the first key step. Take the nucleation and growth of SWCNTs at 900 K employing a Fe_{50} cluster as catalyst as an example,[1] as seen in Figure S1, we can divide the nucleation of SWCNTs into three different stages. The first one is the carbon atom dissolution stage, during which there are many carbon atoms dissolved in the Fe_{50} cluster. With more and more carbon atoms being dissolved into the catalyst, the carbon concentration keeps increasing till a highly-supersaturated state is obtained. This is the second stage, during which some of the carbon atoms

precipitated on the surface of cluster can still dissolve back into it. After that, the precipitated carbon atoms start to nucleate into carbon strings only when the maximum carbon concentration has been obtained, during which time there is a decrease of the carbon concentration inside the cluster. The carbon polygons (or carbon strings) will not dissolve back into the clusters and begin to nucleate into larger graphitic islands as they are more stable than the isolated carbon atoms. When the temperature is sufficiently high, the kinetic energy of carbon islands can be large enough to overcome the attraction from the cluster surface and make the islands lift off from the surface. After that, the carbon concentration in the cluster will keep constant, remaining a supersaturated state. This is the third stage, during which the precipitation rate of carbon atoms is the same with their dissolving-back rate into the cluster. The diameter of the graphite cap keeps increasing with the carbon atoms joining at its open end, until it is as large as that of the cluster. Besides, the length of the SWCNT remains increasing as more and more carbon atoms precipitated onto its open end. Some exposed areas are found to be indispensable to retain the continued growth of the cap structure into a SWCNT.[2] It should be pointed out that the cap diameters are not necessarily the same with that of clusters due to the fact that the practically employed catalyst clusters are not ideally spherical.

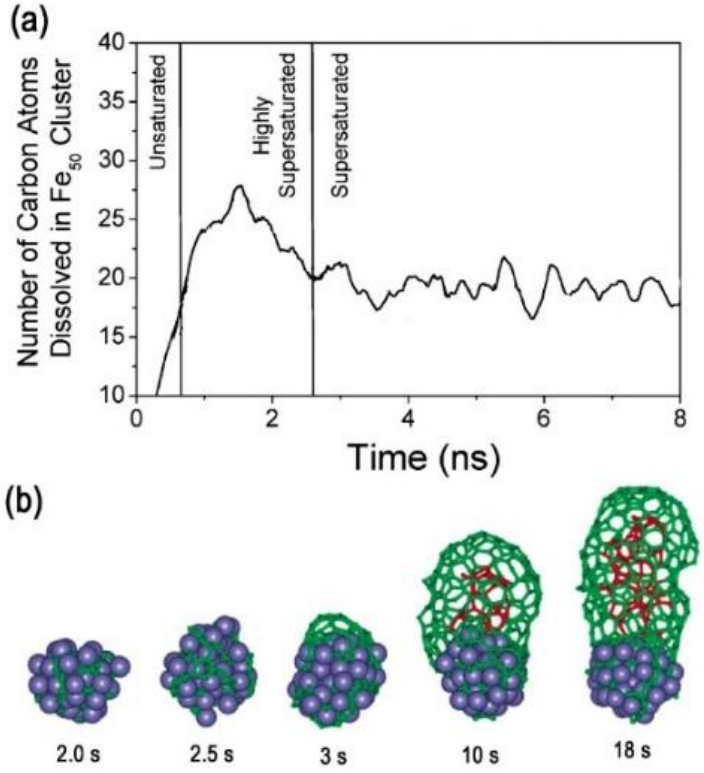

Figure S1. (a) The time dependence of the dissolved carbon content during the nucleation process of a SWCNT. (b) Snapshots during a SWCNT growth at 900 K. (a-b) Reprinted with permission from ref [1]. Copyright 2004 American Chemical Society.

1.1.2 The cap formation of CNTs

The cap structure formation is a very important step in the nucleation process. It is found that there are several different possible routes about how the graphitic islands on the cluster surface form SWCNT caps.[1-3] Although there are usually several graphite islands on the cluster surfaces, generally, only larger cap structures can be found to lift off from the cluster surface while smaller ones cannot be lifted off because of the high curvature energy.[2] Balbuena *et al.* found that, in order for the easy lifting off of the cap structures, the carbon-metal

adhesion should be weak enough to make the curvature energy of the cap structures was smaller than that of SWCNTs with the same diameters.[4] Besides, neither theoretical or experimental observations have been obtained that two or more SWCNTs could coexist on one cluster surface.[5] Morokuma *et al.* found that there were three sequential and repetitive stages for the SWCNT cap nucleation and annealing processes.[6] The metal particle was found to be a key factor in preventing the growing cap structure from forming a closed fullerene cage and keeping the carbon edge active for the continued growth of SWCNTs.[6]

1.1.3 The carbon addition and extension of CNTs

The continuous carbon addition is crucial for the continuous growth of CNTs. During this process, it is critical to maintain a stable carbon addition. It was found that carbon atoms and short chains (*e.g.*, C_2, C_3, and C_4) were assembled into the cap structure through surface or sub-surface diffusion on the cluster (Figure S2a and b).[7] Only pentagons and hexagons (which are short-lived and infrequent) are consisted in the newly formed rings. Morokuma *et al.* observed rapid carbon atom insertion into CNT-Fe interface and short bridging C- and C_2-extensions of CNT were given that an abundant supply of carbon atoms was provided (Figure S2c).[8] The rapid formation of 5-, 6-, 7- and even 8-membered carbon rings contributed the continued CNT growth. Ding *et al.* found that there was a significant barrier for incorporating C atoms into the CNT wall (which is *ca.* ~2 eV for catalysts such as Fe, Co, Ni, *etc.*).[9] Therefore, the incorporation is the threshold step for the CNT growth in most cases.

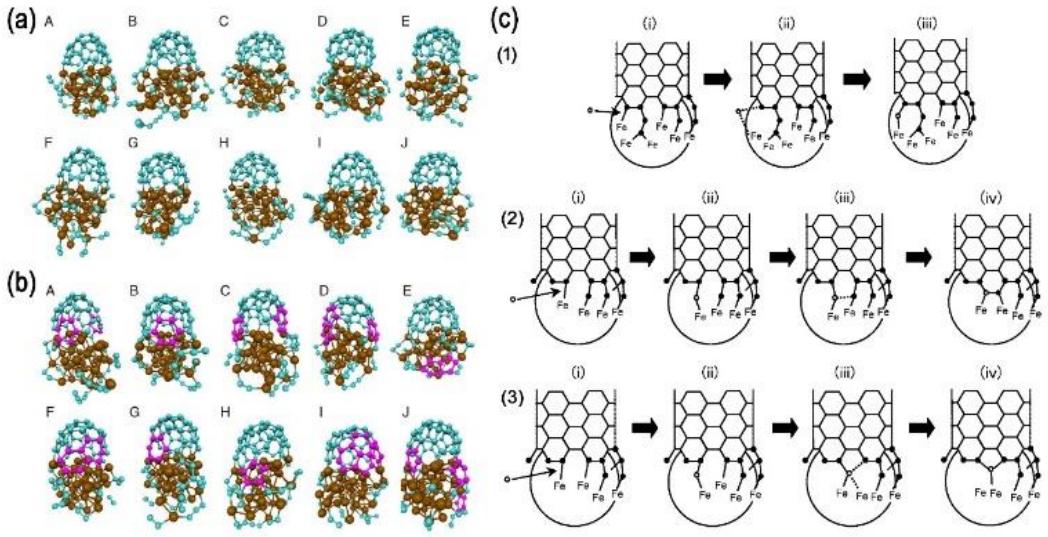

Figure S2. (a) Snapshots of 10 trajectories after 20 ps carbon supply simulations at T=1500 K. (b) Snapshots of 10 trajectories after additional 160 ps carbon-diffusion simulations at T=1500 K. Pink spheres highlight newly formed polygonal carbon rings. (c) Schematic depiction of growth process: (1) incorporation of the incident C into the C-Fe boundary of the CNT-Fe cluster; (2) the six-member ring formation, and (3) the five-member ring formation. (a-b) Reprinted with permission from ref 7. Copyright 2009 Elsevier. (c) Reprinted with permission from ref 8. Copyright 2008 American Chemical Society.

1.2 Factors affecting the nucleation and growth of CNTs

1.2.1 Effect of metal cluster size on nucleation and growth of CNTs

It is widely known that the diameters and other structures of CNTs can be tuned via controlling the catalyst sizes.[11] Generally, the smaller the catalyst sizes are, the smaller the CNT diameters are. Ding *et al.* studied how the catalyst particle sizes affected the formation and structures of CNTs.[10] Figure S3a shows that the Fe_{10} cluster-catalyzed SWCNTs had the worst structures as there were still many

dangling bonds on them. Compared with Fe_{10} cluster, the Fe_{15} cluster-catalyzed SWCNTs had better structures although some dangling bonds still existed. The Fe_{10} and Fe_{15} clusters were not large enough to completely cover the open ends of SWCNTs, resulting in their relatively poor structures. The inserted carbon atoms could not be able to uniformly added to the CNT-cluster interface, thus producing the poor structures of CNTs. The structures of SWCNTs catalyzed by clusters with 20–100 Fe atoms were much better than those grown on smaller Fe clusters. The relationship between SWCNT diameters and cluster diameters is shown in Figure S3b.

1.2.2 Effect of temperature on the nucleation and growth of CNTs

Temperature affects the activity of metal catalysts and thus is an important factor affecting the nucleation and growth of CNTs.[1, 11, 12] Generally, graphene sheets form at temperature < 600 K, while SWCNTs grow at 800~1400 K but soot-like structures are generated when temperature is higher than 1600 K. As shown in Figure S3c and d, when the temperature is low, there will be no sufficient kinetic energy to overcome the C-metal adhesion to make the graphitic islands lifted off from the catalyst clusters, resulting in the formation of graphene sheets on the catalyst surfaces. When the temperatures ranges from 800~1400 K, there is sufficiently high kinetic energy to overcome the above mentioned adhesions to lift the graphitic islands off to form carbon caps which eventually grow into SWCNTs. However, when the temperature is higher than 1600 K, soot-

like amorphous structures will form due to the appearance of many defects in the growing CNTs.

1.2.3 Effect of carbon-metal adhesion on the nucleation and growth of CNTs

It is widely known that the catalyst metal particles have several important functions such as feedstock decomposition, facilitating the nucleation of CNTs, healing defects during CNT growth, and dissolving carbon source species. In addition, another crucial role of the catalyst metal particles is to maintain the open ends of growing SWCNTs.[13, 14] As shown in Figure S3e, it is found that only when the CNT-metal adhesion is comparable to the CNT cap formation energy, can the open ends of CNTs be maintained. For a weak CNT-metal adhesion intensity, the growth of CNTs becomes discontinuous due to the existence of dangling bonds on the open ends. The instability of dangling bonds also accounts for the fact that SWCNTs generally have one open end attached to the catalyst particle and one free-standing closed end.[15-17] The most-often used catalysts such as Fe, Co, and Ni, are found to have higher adhesion than Cu, Pd, and Au and are more efficient for catalyzing CNT growth. However, the CNT-metal adhesion should not be too strong, otherwise it will lead to the diameter increase of CNTs and the formation of discontinuous CNT structures. Figure S3f summarizes three different scenarios that depend on the different CNT-metal adhesion intensity. Morokuma *et al.* discovered that the growth velocity of CNTs grown on the Ni_{55} particles was 69% higher than those grown on Fe_{55} particles

due to the relatively weak Ni-C interaction.[18] Duan *et al.* found that the bonding of zigzag CNTs to metal clusters was higher than that of armchair CNTs.[19]

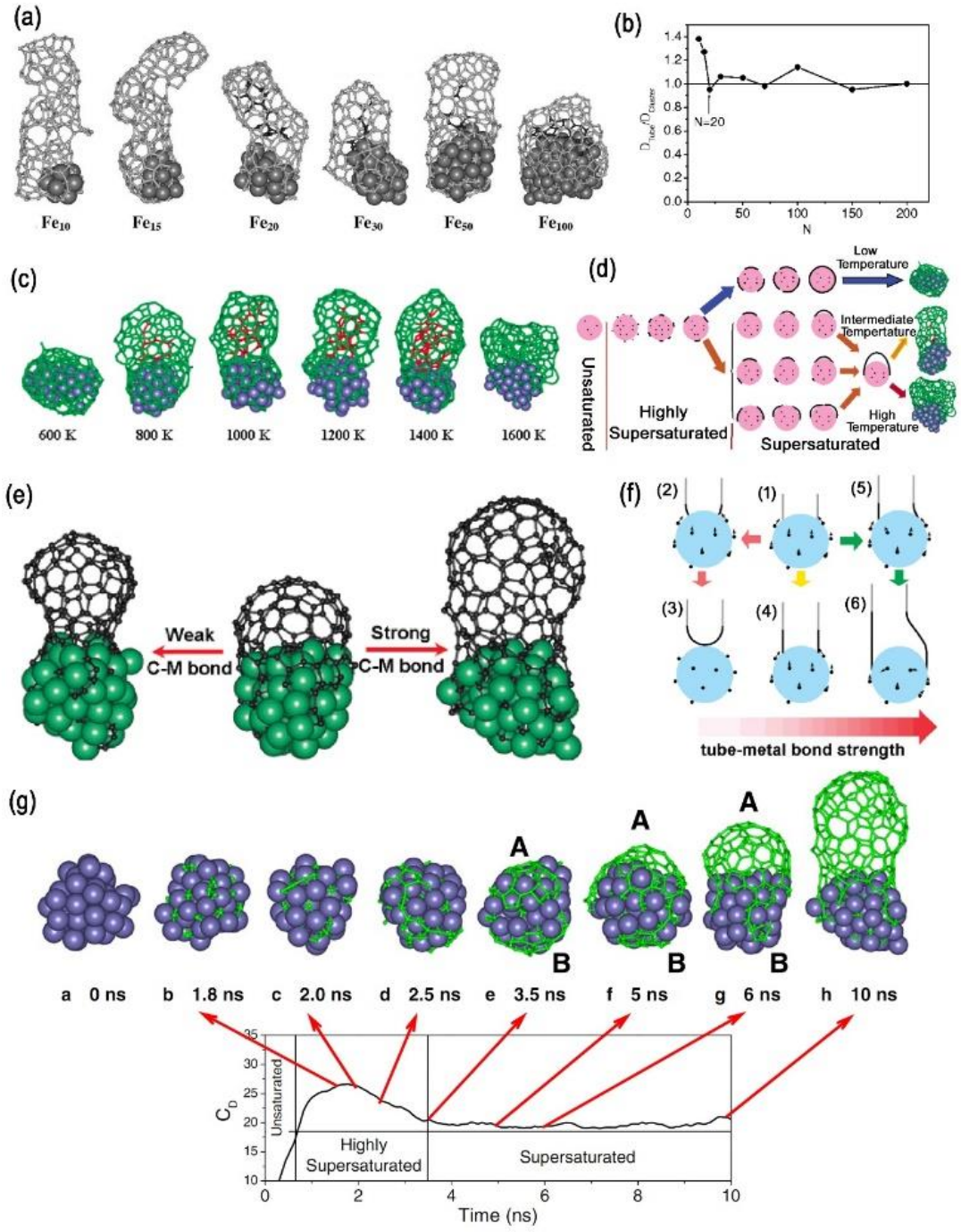

Figure S3. (a) Dependence of the SWCNT structure and diameter on cluster size. The five panels (from left to right) show typical structures that were obtained from clusters containing 10, 15, 20, 30, 50, and 100 Fe atoms, respectively. (b)

Dependence of the SWCNT diameter, D_{Tube}, on the Fe_N cluster diameter, $D_{Cluster}$, for $10<N<200$. The solid line is a guide for the eyes. (c) Graphene (600 K), SWCNT (800-1400 K) and soot (1600 K) structures obtained between 600 and 1600 K. (d) Detailed vapor liquid solid model of SWCNT growth at different temperatures. (e) MD simulations of SWCNT growth with different carbon−metal interaction strengths. (f) Three possible SWCNT growth scenarios from a catalyst particle: I (1→2→3), the nanotube forms a closed cap; II (1→4), the nanotube elongates without a change in diameter; and III (1→5→6), the nanotube elongates and the diameter approaches that of the catalyst particle. (g) Typical SWCNT nucleation and growth as revealed by molecular dynamics simulations. (a-b) Reprinted with permission from ref 10. Copyright 2004 AIP Publishing. (c-d) Reprinted with permission from ref 1. Copyright 2004 American Chemical Society. (e-f) Reprinted with permission from ref 20. Copyright 2008 American Chemical Society. (g) Reprinted with permission from ref 21. Copyright 2006 IOP Publishing Limited.

1.2.4 Effect of carbon concentration and distribution on the nucleation and growth of CNTs

It is found that a highly supersaturated carbon concentration is required to nucleate the formation of the initial small carbon islands precipitated on catalyst surface.[21] A lower yet supersaturated carbon concentration is necessary to make the sizes of the carbon island increase, resulting in the decrease of carbon concentration (Figure S3g). Moreover, in addition to the carbon concentration

and distribution, the carbon atom position in the carbon source molecular also effects the SWCNT formation. Maruyama *et al.* traced the position of carbon atoms during the SWCNT formation employing isotopically labeled ethanol, *e.g.*, $^{12}CH_3$–$^{13}CH_2$–OH.[22] It was found that the carbon away from the hydroxyl group was more preferential than other carbon atoms to be incorporated into the SWCNT structure. Many factors such as the growth temperature, secondary catalyst metal species and the substrates could significantly affect this preference.

1.3 Screw-like dislocation theory of CNT growth

CNTs can be viewed as a kind of crystals that have a screw dislocation along their axis (Figure S4a-d).[23] According to this screw-like dislocation theory, any chiral SWCNT can be viewed as a basic zigzag one, but with a "defect"-through the center-hollow screw dislocation. The SWCNT growth is driven by a free energy decrease $\Delta G(N) = -\Delta\mu \cdot N$ with a number N of added C-atoms ($\Delta\mu$ is the chemical potential drop between the dissolved C atoms in the catalyst and their bound state in the CNT lattice). For achiral SWCNTs (zigzag SWCNTs), it requires a high amount of energy to add a new carbon atom to the completely closed CNT end-edges (Figure S4e). With the carbon atom number increasing, the energy for adding each atom gradually decreases. For adding the last carbon atom to form a complete new tubal end-edge, the corresponding energy is the lowest. However, for the next new CNT end-edge, the energy for adding the first carbon atom will then be much higher than that for adding the last carbon atom.

However, for the chiral CNTs, the case is different. The energy for adding the first atom to a new tubal end-edge in chiral CNTs is much lower than that in achiral CNTs because of the screw dislocation of chiral CNTs, which makes the growth of chiral CNTs much easier than that of achiral CNTs. Many reports have shown that for CNTs synthesized with different methods, those with larger chiral angles have higher abundance (Figure S4f).[24-27] That is to say, the larger the chiral angles, the easier the CNT growth is. Maruyama *et al.* reported the first experimental measurements of growth rates of individual SWCNTs through in situ Raman spectroscopy and correlated them with their chiral angles.[28] They found that the growth rates were directly proportional to the chiral angles (Figure S4g).

As a direct experimental confirmation of screw-like dislocation theory, Purcell *et al.* directly observed the growth of individual SWCNTs from their nucleation stage and found that the SWCNTs often rotated axially during their growth process (Figure S4h-j).[29] It is found that the CNT rotated ~180 times in a 11 minutes growth process. The CNT rotation goes with a ration speed of 24 steps/rotation, which is half the number of atoms on the circumferences of common SWCNTs. Besides, Wei *et al.* found that most of the centimeters long CNTs exhibited a preference of large chiral angles.[30] Ding *et al.* also found that the growth of DWCNTs followed the dislocation-based theory.[31] It is believed that that the C-C bond rotation in a sp^2 carbon network is a crucial step of such a transformation.[32-34] In addition to CNTs, Morin *et al.* showed that the growth of

other nanotubes, such as zinc oxide nanotubes, was also driven by such axial screw dislocations.[35]

Although the screw-dislocation theory fits well with many experimental observations, it should be noted that the precondition for the validity of the screw dislocation theory is that, the threshold step of CNT growth is the direct incorporation of carbon atoms into a CNT wall.[9] For the incorporation of carbon atoms into the CNT walls, there is a significant barrier (~2 eV for common catalysts, *e.g.*, Fe, Co, and Ni), which is obviously higher than the barriers of carbon diffusion on metal surfaces (<1.0 eV)[15, 36-39] and that of the carbon feedstock decomposition (<1.5 eV).[37, 40-42] Therefore, it is found that the incorporation of carbon atoms into a SWCNT wall is the threshold step in most experiments.

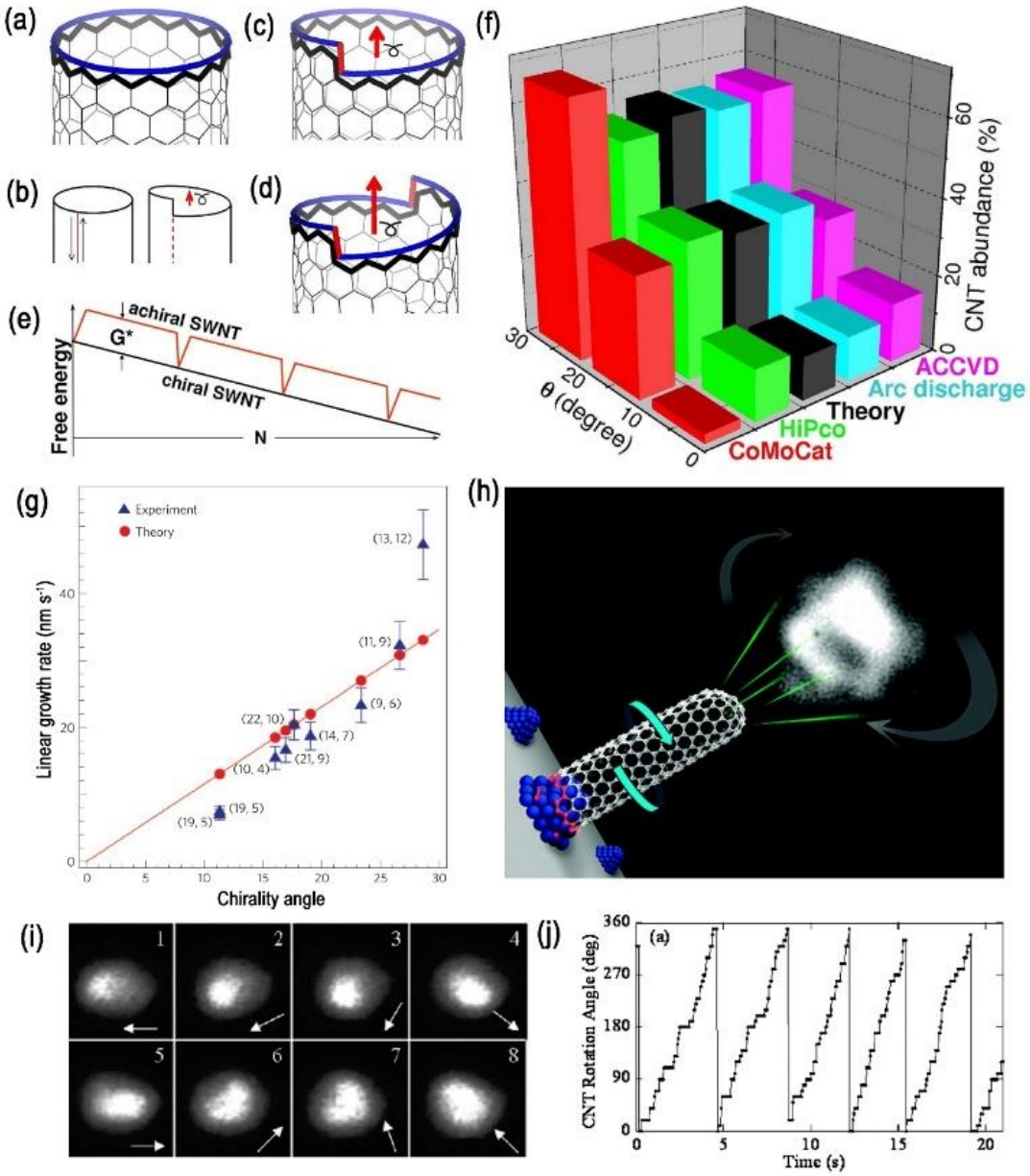

Figure S4. (a-f) An axial screw dislocation in the CNT. An achiral zigzag (n, 0) CNT can be viewed as a perfect crystal, and transformed into a chiral one by cutting, shifting by a Burgers vector b (red arrows in b–d), and resealing a CNT-cylinder (b). The chiral (n, 1) in (c) and (n, 2) in (d) tubes contain the axial screw dislocations with a single and double value of b, accordingly; the corresponding kinks at the open CNT-end are marked in red. (e) Free energy profile during the growth of a chiral or achiral CNT. (f) The distribution of CNT product as a

function of chiral angle. Experimental data of CoMoCat,[25, 26] HiPco,[25] arc discharge,[24] and ACCVD,[24, 25, 27] are extracted from literature. θ is the chiral angle of CNTs. (g) The linear growth rates (blue triangles) along with assigned (n, m) chiral indices are plotted against the chiral angle. (h) Schematic illustration showing a SWCNT rotating during growth. (i) Sequence of FEM patterns from a growing CNT that follows a single revolution as the CNT lengthens (in the order of 1 to 8). (j) Frame by frame measurement of the rotation angle of the pattern showing that it proceeded step by step. The number of the steps for the five cycles are (25, 25, 21, 21, 25) varying because rotations over one or less frames are difficult to tabulate. (a-f) Reprinted with permission from ref 23. Copyright 2009 National Academy of Sciences. (g) Reprinted with permission from ref 28. Copyright 2012 Nature Publishing Group. (h-j) Reprinted with permission from ref 29. Copyright 2009 American Chemical Society.

1.4 Non-metal catalyzed growth of CNTs

Although the transition metal nanoparticles are efficient catalysts for CNT growth, the existence of metal nanoparticles also brings many restrictions to the application of HACNTs, especially in the field of micro/nano-electronics. Besides, the removal of metal residues is another problematic issue. On many occasions, it is very difficult to completely remove the metal residues. In order to avoid the problems caused by the metal catalysts, non-metal catalyzed growth of CNTs were proposed. In this section, we give a brief introduction of the non-metal catalyzed CVD growth of HACNT.

1.4.1 Growth mechanism of CNTs using non-metal catalysts

It has been widely believed that the CNT grown from non-metal catalyst such as SiO_2 nanoparticle followed by a vapor-solid (VS) mechanism, which was different from metallic catalysts.[43, 44] Similarly, Cheng *et al.* proposed a vapor–solid–solid (VSS) mechanism to interpret the non-metal catalyzed growth of CNTs from SiO_x.[45] During the CNT growing process, the active catalysts were found to be the amorphous solid SiO_x nanoparticles. In addition to the effect of catalyst sizes, oxygen was also found to be a crucial factor affecting the CNT growth in the VSS mechanism, which was confirmed by the *in situ* TEM observations. Homma *et al.* found that the solid nanoparticles could become the carbon coated nanoparticles during the CNT growth.[46] During the growth of CNTs, graphene islands with pentagon rings were formed on the carbon saturated catalyst surfaces as the nucleuses of CNTs.[47] Chen *et al.* found that there was only low energy barriers towards the incorporation of C atoms or C_2 dimers during the CNT growth based on non-metal catalysts.[48]

1.4.2 Controlled growth of non-metal catalyzed CNTs and the factors affecting their growth

The reports of non-metal catalyzed growth of CNTs were as early as in 2002, when Avouris *et al.* reported the hexagonal silicon carbide catalyzed growth of SWCNTs at 1500 °C (Figure S5a-d).[49] It should be noted that the growth velocity of non-metal catalyzed CNTs is very low. Cheng *et al.* found that the growth speed of SiO_2 nanoparticles catalyzed SWCNTs was only 8.3 nm/s, 300~600 times lower than

the metal catalyzed CNT growth.[50] Such a slow growth velocity makes the length-controlled CNT growth, especially the short CNTs with length of hundreds of nanometers, possible and feasible. Generally, the synthesis of non-metal catalyzed CNTs is simple, especially compared with the metal catalyzed synthesis of CNTs. For example, Cheng *et al.* obtained high-quality dense and uniform SWCNTs using a 30-nm-thick SiO_2 sputtered Si/SiO_2 wafer as substrate and methane as a carbon source (Figure S5e and f).[51] By scratching a clean Si/SiO_2 wafer using another wafer with a sharp tip to get desired patterns (Figure S5g and h), SWCNTs would grow in the scratched zones. Huang *et al.* demonstrated that SiO_2 nanoparticles could be produced by simply scratching the quartz or silicon wafer using a SiO_2 layer and confirmed these nanoparticles were active for growing SWCNTs (Figure S5i-l).[52] In addition to the SiO_2 nanoparticles, a series of other oxides such as Al_2O_3, TiO_2, Cr_2O_3, ZnO and ZrO_2 and even rare earth oxides were also found to be active for synthesizing SWCNTs (Figure S5m and n).[53] Homma *et al.* found that the pretreatment of the SiO_2 in H_2 at high temperature (> 950 ^oC) was critical for the effective growth of SWCNTs.[47] It was found that by annealing the SiO_2 substrates at high temperature in H_2 atmosphere, many defects were generated on their surfaces, which provided many nucleation sites for the SWCNT growth. In addition to the oxide nanoparticles as the catalyst, fullerene could also be used as the non-metal catalyst. Zhang *et al.* reported the structure-controlled synthesis of SWCNTs using C_{60} caps as catalysts.[54] The cap structures and sizes could be tuned by varying the thermal oxidation temperature. Zhou *et al.* used $C_{50}H_{10}$ to grow SWCNTs.[55] The dehydrogenated $C_{50}H_{10}$ molecules facilitate chirality-selective growth

of SWCNTs. This cap engineering using opened fullerenes shows great potential for the structure-controlled synthesis of SWCNTs.

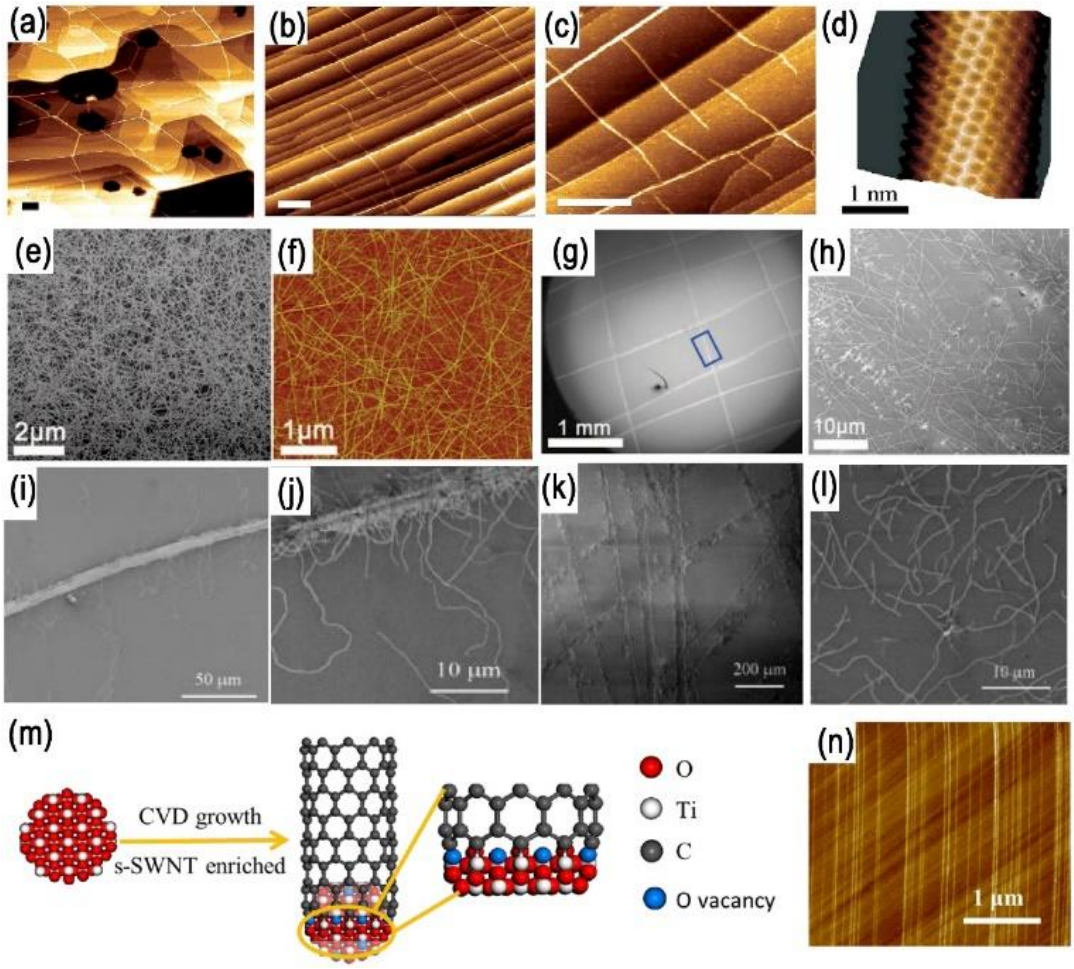

Figure S5. (a-c) STM images of two SiC samples after a 1650 °C annealing in vacuum. Scale bars: 250 nm. (d) Atomic resolution STM image of a single carbon nanotube. (e) Typical SEM and (f) AFM images of the as-grown SWCNTs on Si/SiO_2 substrate covered with a 30-nm-thick sputtering deposited SiO_2 film. (g) SEM image of the SWCNTs grown on a cross patterned Si/SiO_2 wafer. (h) Enlarged SEM images of the blue square area in image a, showing that SWCNTs are grown at the scratched positions, while no SWCNTs are found in the unscratched areas. (i-l) SEM images of SWCNTs from the scratched substrates

by diamond blade after CVD at 900 °C for 10 min: (i-j) Si wafer with 1 μ SiO_2 layer at different positions; (k-l) quartz plate with different magnifications. (m) Schematic illustration of selective growth of semiconducting SWCNTs by TiO_2 nanoparticles; (n) AFM images of the SWCNT arrays using TiO_2 nanoparticles as catalysts. (a-d) Reprinted with permission from ref 49. Copyright 2002 American Chemical Society. (e-h) Reprinted with permission from ref 51. Copyright 2009 American Chemical Society. (i-l) Reprinted with permission from ref 52. Copyright 2009 American Chemical Society. (m-n) Reprinted with permission from ref 53. Copyright 2015 American Chemical Society.

Supplementary Text S2

2. Manipulation of CNTs

2.1 AFM-based manipulation of individual CNTs

AFM is a powerful tool to manipulation CNTs with relatively high resolution. AFM tips have two kinds of movements: vertical movements and lateral movements, which produces vertical forces and lateral forces accordingly.[56] Both vertical and lateral movements can be realized with piezoelectric elements. The working modes of AFM tips can be divided into three types: contact mode, tapping mode and non-contact mode. The contact mode can be used for manipulation while the tapping and non-contact mode can attain higher imaging resolution.[57] The imaging and manipulation of CNTs can be

performed within the same experiment.[58] Moreover, CNTs can be imaged and manipulated under ambient conditions, while the manipulation in SEM and TEM must be performed with high or ultrahigh vacuum. AFM can be used to manipulate the alignment, shape and position of individual CNTs dispersed on a substrate.[59-61] For instance one can bend, straighten, translate, rotate, and sometimes cut CNTs (Figure S6a-e). Such manipulations are feasible due to the interaction between nanotubes and the substrate, which can stabilize highly strained nanotubes configurations.[62] Besides, AFM was also used to study the controlled rolling of CNTs on graphite surface to investigate their nanoscale movement.[63] Tapping mode of AFM can also be employed to investigate the radial deformability of a CNT.[64] An AFM operating in air was employed to exert a load to a CNT and to directly determine the resulting deflection (Figure S6f-g).[65] In addition, AFM manipulation also facilitates the electrical measurement of individual CNTs. As shown in Figure S6h-m, by AFM tip manipulating the CNTs dispersed on a substrate with metal electrodes, the CNTs can be placed such that they can bridge the two electrodes and their I-V characteristics can be evaluated.[61]

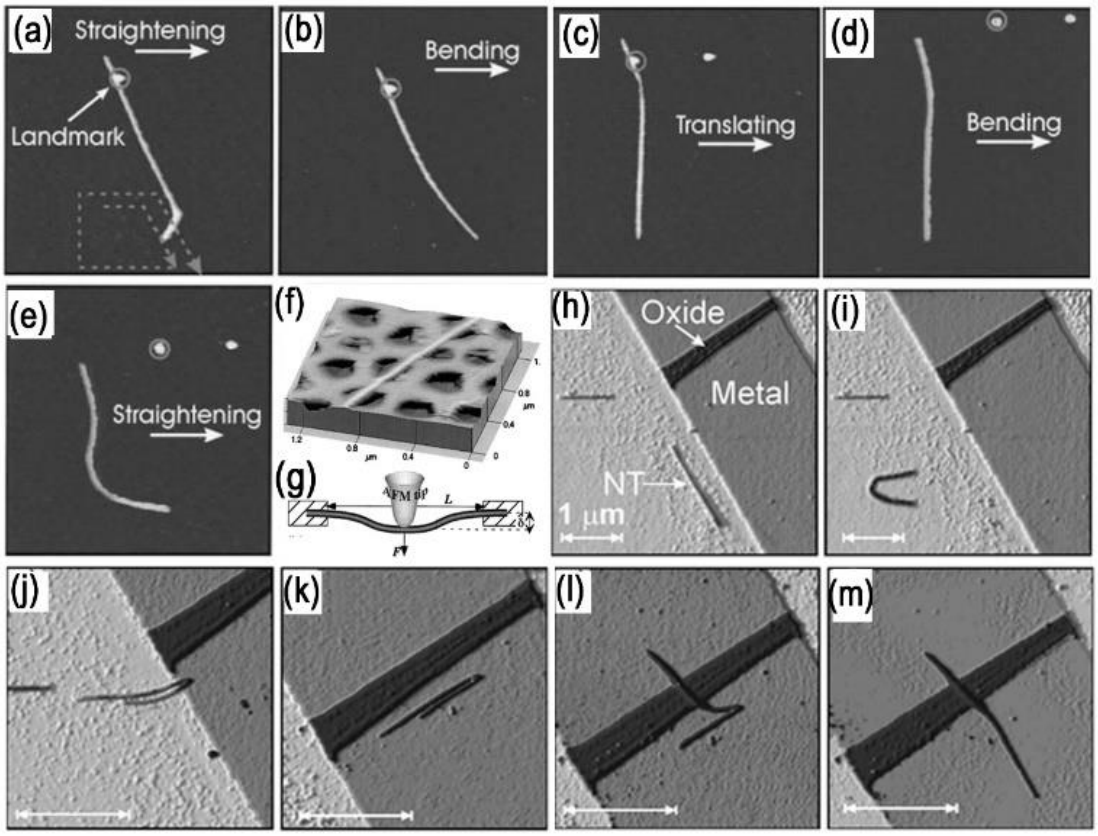

Figure S6. (a-e) Manipulation of a 0.9 μm long and 80 Å high CNT at a vertical load of 20 nN. (f) AFM image of a CNT rope adhered to a polished alumina ultrafiltration membrane, with a portion bridging a pore of the membrane. (g) Schematic of the measurement: the AFM was used to apply a load to the nanobeam and to determine directly the resulting deflection. (h-m) AFM manipulation of a CNT such that electrical transport through it could be studied. (a-e) Reprinted with permission from ref 62. Copyright 1998 American Chemical Society. (f-g) Reprinted with permission from ref 65. Copyright 1999 American Physical Society. (h-m) Reprinted with permission from ref 61. Copyright 1999 Elsevier.

2.2 TEM-based manipulation of individual CNTs

During the past years, nanomanipulator systems have been developed for the characterization and manipulation of CNTs with nanometer-scale resolution as well as multiple degrees of freedom with both position and orientation control, independently actuated multiprobes, and a real-time observation system.[57, 66] A nanomanipulator installed in a TEM could perform 3-D nanomanipulation of individual CNTs. Zettl *et al.* reported an in situ method for controlling the shape and morphology of CNTs in TEM.[67] The shaping process involves the electrically driven vaporization of successive layers of the MWCNTs, with outer layers being removed in turn near the end of the CNT, leaving the core CNT walls intact and protruding from the bulk of the CNT. Ren *et al.* reported the atomic scale imaging of the breakdown of single CNTs in a TEM equipped with a nanomanipulator.[68] Peng *et al.* developed a method to shape CNTs into desired morphology while maintaining its electrical and mechanical properties (Figure S7a-d).[69] The CNTs can be cut, manipulated, and even soldered via a nanomanipulator fixed in TEM (Figure S7e-h).[70] The solder of CNTs was realized through the deposition of amorphous carbon accumulated at the CNT junction.[71] All CNT structures, including simple tube-tube connections, crossed junctions, T-junctions, zigzag structures, and even CNT networks could be constructed with a high degree of control, and their electrical and mechanical properties could be measured in situ inside the TEM. Similar experiment was also employed to detect the mechanical properties of WS_2 nanotubes[72] and the electrical properties of Boron Nitride nanotubes[73] in TEM. Besides, in situ TEM positive field evaporation experiments were conducted for grinding

CNTs.[74] They also used a CNT nanoknife adhere to a metal tip to precisely cut and to sharpen CNTs.[75]

2.3 SEM-based manipulation of individual CNTs

Compared with TEM, SEM has a much larger operation space for the characterization, measurement and manipulation of CNTs although the resolution of SEM is relatively low. The SEM-based nanomanipulators have more DOFs than that based on TEMs and can conduct a series of functions to characterize and manipulate CNTs.[76] Figure S7i shows a SEM-based nanomanipulator reported by Ruoff *et al.*[76] Using this nanomanipulator, the tensile strengths of individual MWCNTs were measure within a SEM (Figure S7j-k).[77] Later, using the same nanomanipulator, they studied the sliding behavior between nested shells of MWCNTs.[78] Peng *et al.* conducted a series of nanomanipulation using a four nanoprobe system inside an SEM.[79] They even developed a "nanoknife" using this system to precisely cut and to sharpen CNTs,[75] measured the tensile strength[80] and the natural frequencies of single MWCNTs us.[81, 82] In addition to the above manipulations, they also realized the contact between CNTs, either sitting on an substrate or suspended, and metal tips for the measurement of I-V characteristics.[83] They found that the in situ mechanical, electrical and electromechanical measurements of CNTs could be performed at the same time by using such a nanomanipulator system (Figure S7l-o).[84] Lim *et al.* also developed a SEM-based nanomanipulation system for individual CNTs.[85] In addition to the above two kinds of nanomanipulator systems, there are still other types of piezo-driven

nanomanipulator systems inside SEM.[86-89] All these nanomanipulations in SEM greatly facilitates the characterization and manipulation of CNTs.

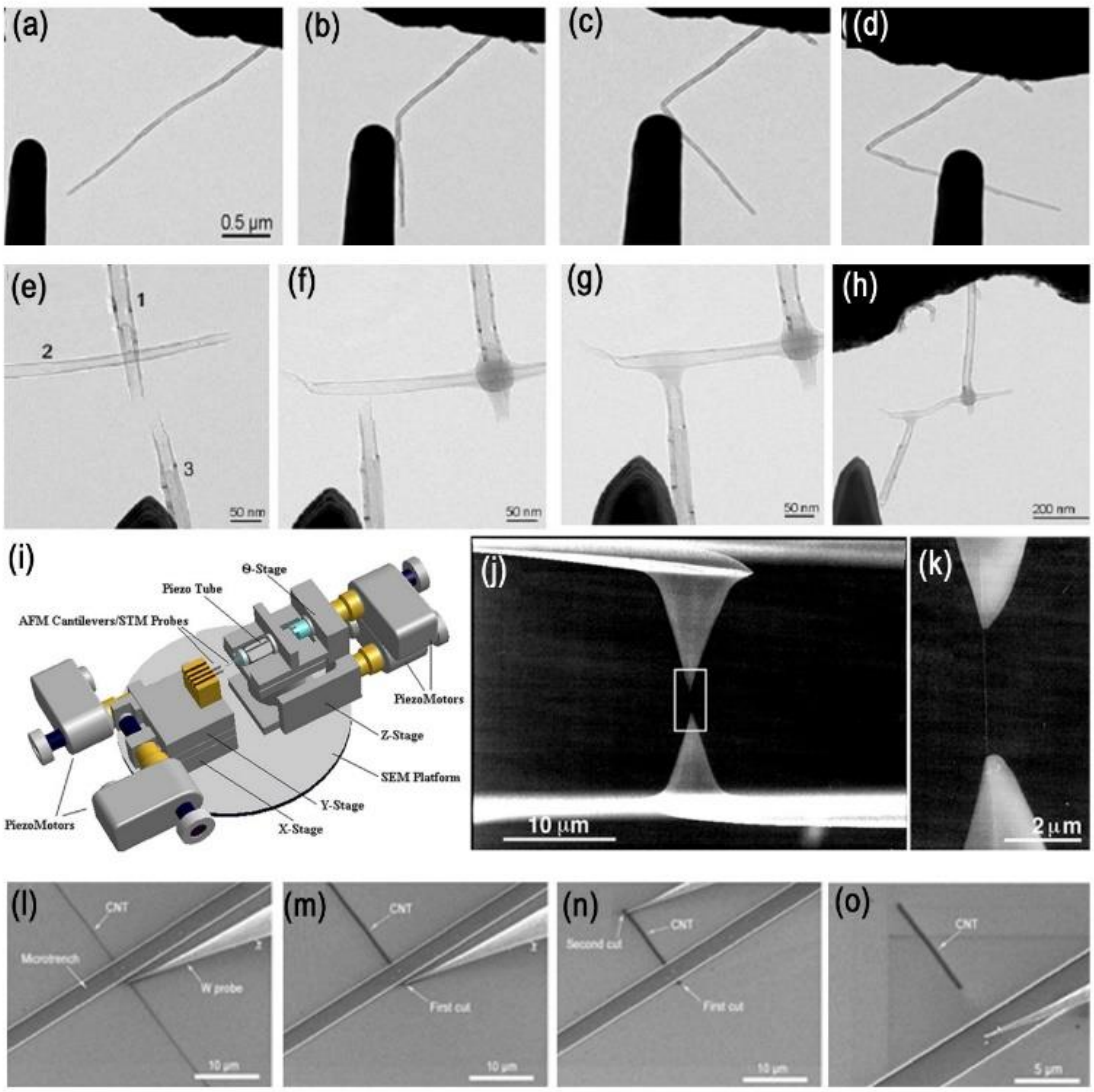

Figure S7 (a-d) A series of TEM images showing the bending process of a typical freestanding CNT via the lateral movement of the W tip (from left to right in the images). (e-h) TEM images showing the fabrication of a simple CNT network consisting of three ruptured CNTs. (i) Schematics of a nanomanipulator inside SEM.[76] (j) SEM image of two AFM tips holding a MWCNT, which was attached at both ends on the AFM silicon tip surface by electron beam deposition of carbonaceous materials. (k) High-resolution

SEM image of the indicated region in (j), showing the MWCNT between the AFM tips. (l-o) SEM images showing the process of picking up a thin CNT from a SiO_2/Si substrate using a tungsten probe. (a-d) Reprinted with permission from ref 69. Copyright 2006 Wiley-VCH. (e-h) Reprinted with permission from ref 70. Copyright 2005 Wiley-VCH. (i-k) Reprinted with permission from ref 77. Copyright 2000 American Association for the Advancement of Science. (l-o) Reprinted with permission from ref 84. Copyright 2010 Elsevier.

Supplementary Text S3

3. Application of individual HACNTs

3.1 Diodes

A diode is a two-terminal p-n junction device used for rectification, which is different from FETs which are three-terminals. In addition to being a rectifier, they should also be infrared light emitting diodes. Semiconducting CNTs are direct band-gap materials and thus are useful for the diodes fabrication. CNT diodes can be fabricated either by using asymmetric gating[90, 91] or by asymmetric contacts.[92, 93] Lee *et al.* demonstrated that individual SWCNTs can form ideal p-n junction diodes (Figure S8a).[91] In 2004, Heller *et al.* reported the fabrication of a SWCNT p-n junction diode device, which fabricated on a CNT via electrostatic doping utilizing a pair of split electrodes (Figure S8b-d).[90] The device could either be an ambipolar FET or be a diode, depending on how the two gates were biased. Both forward conduction and rectification appeared on the current-voltage characteristics of the diode. In 2008, Peng *et al.* reported the

fabrication of an ambipolar FET and a barrier-free bipolar diode utilizing a doping-free CNT-CMOS inverter.[92] This CNT device can function as different devices such as high-performance ambipolar FET, CMOS inverter, n-FET, p-FET, and barrier-free bipolar diode (Figure S8e-g). In the same year, Liu *et al.* presented a controllable approach for fabricating an air-stable SWCNT diode with the AFM manipulation technique (Figure S8h and i).[93] Air-stable SWCNT diodes with rectification ratios of up to 10^4 were generated with this approach. In 2010, Rogers *et al.* reported the fabrication of Schottky diodes based on SWCNT arrays.[94] It is shown that the existence of metallic SWCNTs in the diodes made the rectification ratio (defined as the maximum/minimum current ratio) to be low. In 2011, Peng *et al.* carried out the electroluminescence (EL) measurements on a two-terminal CNT-based light-emitting diode (LED).[95] This two-terminal device is composed of an asymmetrically contacted semiconducting SWCNT (Figure S8j-m). On the one end the SWCNT is contacted with Sc and on the other end with Pd. At large forward bias, with the Sc contact being grounded, electrons are injected barrier-free into the SWCNT conduction band from the Sc contact and holes be injected into the valence band from the Pd electrode. The injected electrons and holes recombine radiatively in the SWCNT channel yielding a narrowly peaked emission peak at 30 meV. In 2012, Peng *et al.* fabricated CNT-based diodes with different channel length between L=0.6μm to 3.5 μm on the same CNT and investigated their electric and photovoltaic characteristics (Figure S8n-r).[96] It is found that although the open voltage of the diode increases rapidly for channel length L less than 1.0 μm, it saturates for longer channel devices. On the other hand, the short circuit current of the

diode exhibits a clear peak at intermediate channel length of about 1.5 μm. The optimal channel length for a CNT diode in photovoltaic application is thus determined to be about 1.5 μm. Besides the HACNTs, they also fabricated diodes based on random networks of SWCNTs.[97] Although sub-10 nm channel length CNT transistors have been demonstrated with superb performance,[98] the scaling of CNT p–n diodes or photodiodes is held back on a scale of micrometers.[90, 91, 99] In 2014, Peng *et al.* demonstrated that CNT diodes fabricated via a dopant-free technique showed good rectifying characteristics and photovoltaic response even when the channel length is scaled to sub-50 nm (Figure S8s-v).[100] By making a trade-off between performance and size, a small diameter CNT-based diode with both channel length and contact width around 100 nm shows a photovoltage of 0.24 V and a fill factor of up to 60%. The transferred charges induced potential barrier at the contact in long channel diodes and the effect of self-adjusting charge distribution has been revealed.

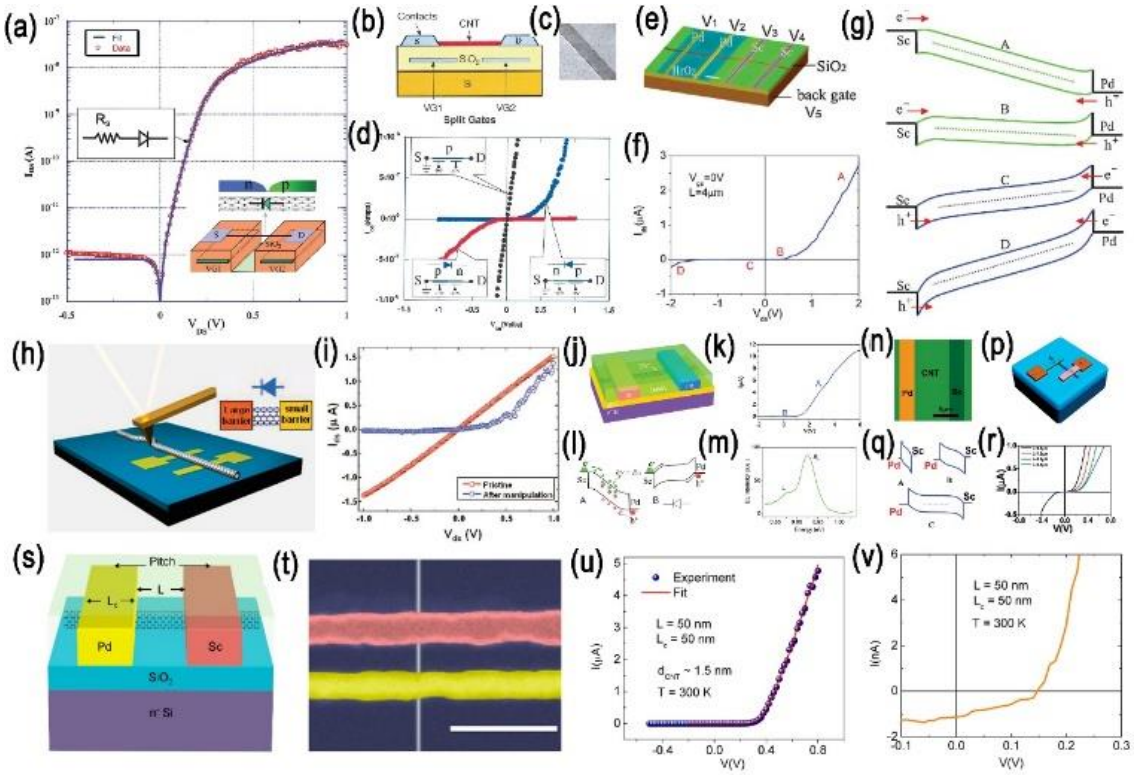

Figure S8. (a) The inset shows the split gate device where VG1 and VG2 are biased with opposite polarities (VG1=−VG2= +10 V) to form an ideal p-n junction diode along a SWCNT. (b) Schematic cross section of SWCNT p-np-n junction diode. (c) SEM of a SWCNT over a 1μm1μm split gate. (d) I–VI–V characteristics of a single SWCNT when electrostatically doped to form a p-n junction, n-p junction, or p channel FET. (e-g) CNT CMOS inverter-based bipolar diode. (h) Schematic illustration of fabricating the SWCNT diode with AFM manipulation. (i) I_{ds}−V_{ds} curves of the SWCNT shown in Figure 57h before and after manipulation at V_g=−10 V. (j) Schematic diagram illustrating the structure of an asymmetrically contacted CNT device. (k) Experimental I−V characteristics of the CNT diode (device 1 with a channel length ~1 μm) showing a typical rectifying behavior of a diode. (l) Band diagrams which correspond to the two representative points A and B of (k). (m) EL spectrum of the

diode when operated at large forward bias with a large diode current I = 7.5 μA. (n-p) Optical microscope image of seven devices with different channel length. (q) Energy band diagram depicting the build-in electric field in short (panel A), immediate (panel B), and long (panel C) channel BFBDs. (r) Current voltage characteristics of four CNT diodes with a diameter of 3.1 nm and channel length L ≈ 0.6 μm (dark), 1.5 μm (red), 2.5 μm (green), and 3.5 μm (blue). (s) Schematic device structure of a SWCNT photodiode with asymmetric contacts. (t) False-colored scanning electron microscope image showing a 100 nm pitch CNT diode with L ≈ L_c ≈ 50 nm. The scale bar is 200 nm. (u) Experimental and fitted I–V rectifying characteristics of the 100 nm pitch diode in the dark and (v) I–V characteristic under illumination at room temperature with a light intensity of 25 KW/cm2. (a) Reprinted with permission from ref 91. Copyright 2005 Elsevier. (b-d) Reprinted with permission from ref 90. Copyright 2004 Elsevier. (e-g) Reprinted with permission from ref 92. Copyright 2008 Wiley-VCH. (h-i) Reprinted with permission from ref 93. Copyright 2008 American Chemical Society. (j-m) Reprinted with permission from ref 95. Copyright 2011 American Chemical Society. (n-r) Reprinted with permission from ref **96. Copyright 2012 American Chemical Society. (s-v) Reprinted with permission from ref 100. Copyright 2014 American Chemical Society.**

3.2 Memory devices

During the past years, some groups have demonstrated the effective fabrication of CNT-based memories, which are based on the hysteresis in the I_{ds}–V_g curve.[101, 102] In 2000, Lieber first proposed the concept for fabricating memories employing CNTs as both

molecular wires and molecular device elements for writing and reading information (Figure S9a-f).[103] They used a suspended and crossed CNT to fabricate the device element with electrostatically switchable ON/OFF states, which were used to fabricate logic function tables and nonvolatile random-access memories at an integration level reaching 10^{12} elements/cm^2. Fuhrer *et al.* fabricated a nonvolatile charge-storage memory element operating at room temperature using a high-mobility (9000 $cm^2/V{\cdot}s$) semiconducting SWCNT transistor (Figure S9g-i).[101] Charges were stored by application of a few volts across the silicon dioxide dielectric between CNT and silicon substrate, and detected by threshold shift of the CNT FET. The high mobility of the CNT transistor allows the observation of discrete configurations of charge corresponding to rearrangement of a single or few electrons. Kern *et al.* fabricated molecular memory devices with semiconducting SWCNTs forming a 150 nm long channel (Figure S9j and k).[102] By sweeping gate voltages in the range of 3 V, data can be stored with a stability of> 12 days at room temperature. Liu *et al.* proposed the fabrication of an electrical switch device with an on/off ratio of 10^3 using two crossed CNTs as the electrodes and Ag-tetracyanoquinodimethane as the electrical bistable medium (Figure S9l-n).[104]

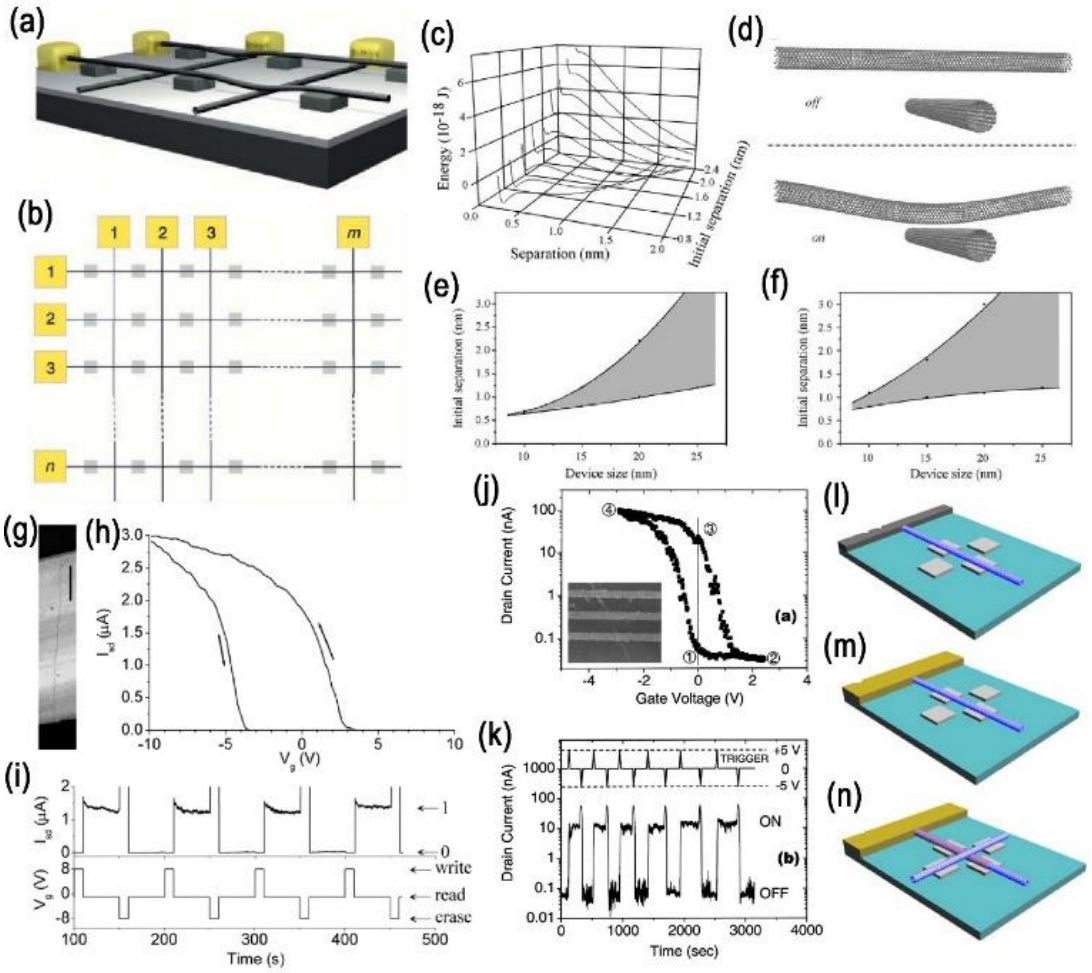

Figure S9. (a) Three-dimensional view of a suspended crossbar array showing four junctions with two elements in the ON (contact) state and two elements in the OFF (separated) state. (b) Top view of ann by m device array. (c) Plots of energy, $E_T = E_{vdW} + E_{elas}$, for a single 20-nm device as a function of separation at the cross point. (**d**) Calculated structures of the 20-nm (10, 10) SWCNT device element in the OFF (top) and ON (bottom) states. (**e** and **f**) Plots of the bistability range for the crossed nanotube elements as a function of device size. (g) AFM (intermittent-contact mode) topograph of the nanotube device used in this study. Scale bar: 1 micron. (h) Drain current as a function of gate voltage at room temperature and a source-drain bias of 500 mV. (i) Four read/write cycles of the nanotube memory at room temperature. (j-

k) Memory effects observed at room temperature in an individual SWCNT with a diameter of ~2 nm. (l-n) Schematics for the fabrication process of the CNT/AgTCNQ/CNT structure. (a-f) Reprinted with permission from ref 103. Copyright 2000 American Associate for the Advancement of Science. (g-i) Reprinted with permission from ref 101. Copyright 2002 American Chemical Society. (j-n) Reprinted with permission from ref 104. Copyright 2008 Elsevier.

3.3 Inverter

The inverter is a device that can change the direct current to the alternating current. In 2001, Zhou *et al.* reported the fabrication of PMOS and CMOS inverters using SWCNT FETs (Figure S10a-e).[105] The PMOS and CMOS inverters were demonstrated separately by using resistor as the load for a p-type CNT FET, and by connecting a p- and n-type CNT transistor, both of the two types of inverters showed good transfer performance at room temperature. In 2007, Peng *et al.* fabricated high performance complementary inverters using SWCNT (Figure S10g-k).[106] The Al_2O_3 top-gate dielectric was grown via first depositing an Al film followed by complete oxidation of the film. It is shown that the quality of the Al_2O_3 film can be significantly improved by annealing at 400 °C, and high-quality p- and n-type CNT FETs may be fabricated utilizing either Pd (p-type) or Al (n-type) electrodes. High performance complementary inverter was demonstrated by integrating the p- and n-type CNT FETs on the same CNT, and a gain of about 3.5 was achieved. They also fabricated ballistic n-type CNT-based FETs by contacting semiconducting SWCNTs using Sc (Figure S10l and m).[107]

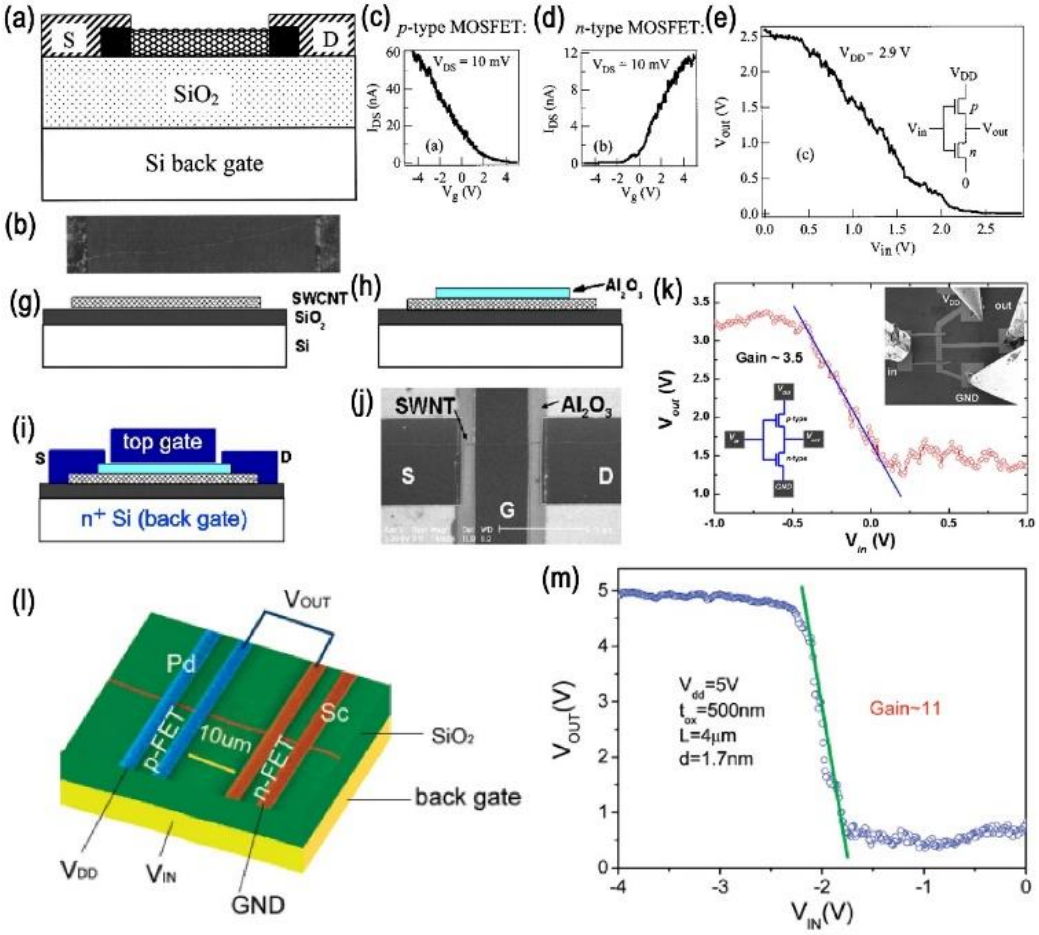

Figure S10. (a) Schematic diagram of the carbon nanotube transistors used in this study. (b) AFM image of a typical device. (c) I-V_g curve for a p-type nanotube transistor. (d) I-V_g curve for an n-type nanotube transistor. (e) Transfer characteristics of a CMOS nanotube inverter constructed by connecting the p-type transistor with the n-type transistor. (g-k) Fabrication process of top-gate CNTFETs. (g) SWCNT was first grown on SiO2 substrate by CVD method, (h) an Al_2O_3 gate insulator layer was then grown on top of the SWCNT, (i) the source, drain, and gate electrodes were patterned by electron beam lithography and lift-off. (j) SEM image showing a typical so fabricated top-gate CNTFET. (k) Transfer characteristics of a complementary voltage inverter fabricated using a single CNT, showing a gain of ~3.5. The upper right inset is a SEM

image of the inverter. (l-m) Back-gated (t_{ox} = 500 nm) SWCNT complementary inverter. (a-f) Reprinted with permission from ref 105. Copyright 2001 Elsevier. (g-k) Reprinted with permission from ref 106. Copyright 2007 Elsevier. (l-m) Reprinted with permission from ref 107. Copyright 2007 American Chemical Society.

3.4 Resonators

High quality resonating systems, providing high frequency resolution and long energy storage time, are crucial in many fields of physics. In particular in the field of NEMS,[108] recent research has led to the development of high frequency top-down fabricated mechanical resonators with high-quality factors.[109-112] However, when mechanical resonators are miniaturized to make them lighter and to increase their resonance frequency, the quality factor tends to decrease significantly from surface effects.[108] High Q values combined with high resonance frequencies are an important prerequisite for applications such as single-atom mass sensing[113-115] and fundamental studies of the quantum limit of mechanical motion.[116] SWCNTs present a potentially defect-free NEMS with extraordinary mechanical properties: in particular, the high Young's modulus (E = 1.2 TPa) in combination with a very low mass density (ρ = 1350 kg/m^3).[114, 117-119] During the past years, a lot of achievements have been obtained in CNT resonators.[109, 113, 114, 118-124] Zant *et al.* fabricated a frequency mixer using a suspended CNT to measure its mechanical motion (Figure S11a-e).[118] A single gate-dependent resonance with Q-factors between 6 and 300 and frequencies ranging from 20 to 100 MHz was observed. The transversal vibration mode of suspended CNTs was also observed at millikelvin temperatures.[122] Kouwenhoven *et al.* measured the

mechanical resonances of a suspended CNT via electrical mixing in the device (Figure S11f-h).[121] A sequence of modes extending to 39 GHz was observed with a quality factor of 35 000 in the highest mode. This unprecedentedly high combination corresponds to a thermal excited state probability below 10^{-8} and a relaxation time of 140 ns with microsecond relaxation times for lower modes. In order to achieve mass measurement of biological molecules in viscous fluids using CNT resonators, Arie *et al*. investigated the vibration of nanotube cantilevers in water using the optical detection technique (Figure S11i-n).[123] It was found that the nanotube lost its fundamental oscillation once immersed in water, suggesting a great viscous resistance to the nanotube vibration in water. The resonant frequency of the nanotube in water decreased with lowering the water temperature, corresponding to the natural phenomenon by which liquid viscosity tends to increase at lower temperatures.

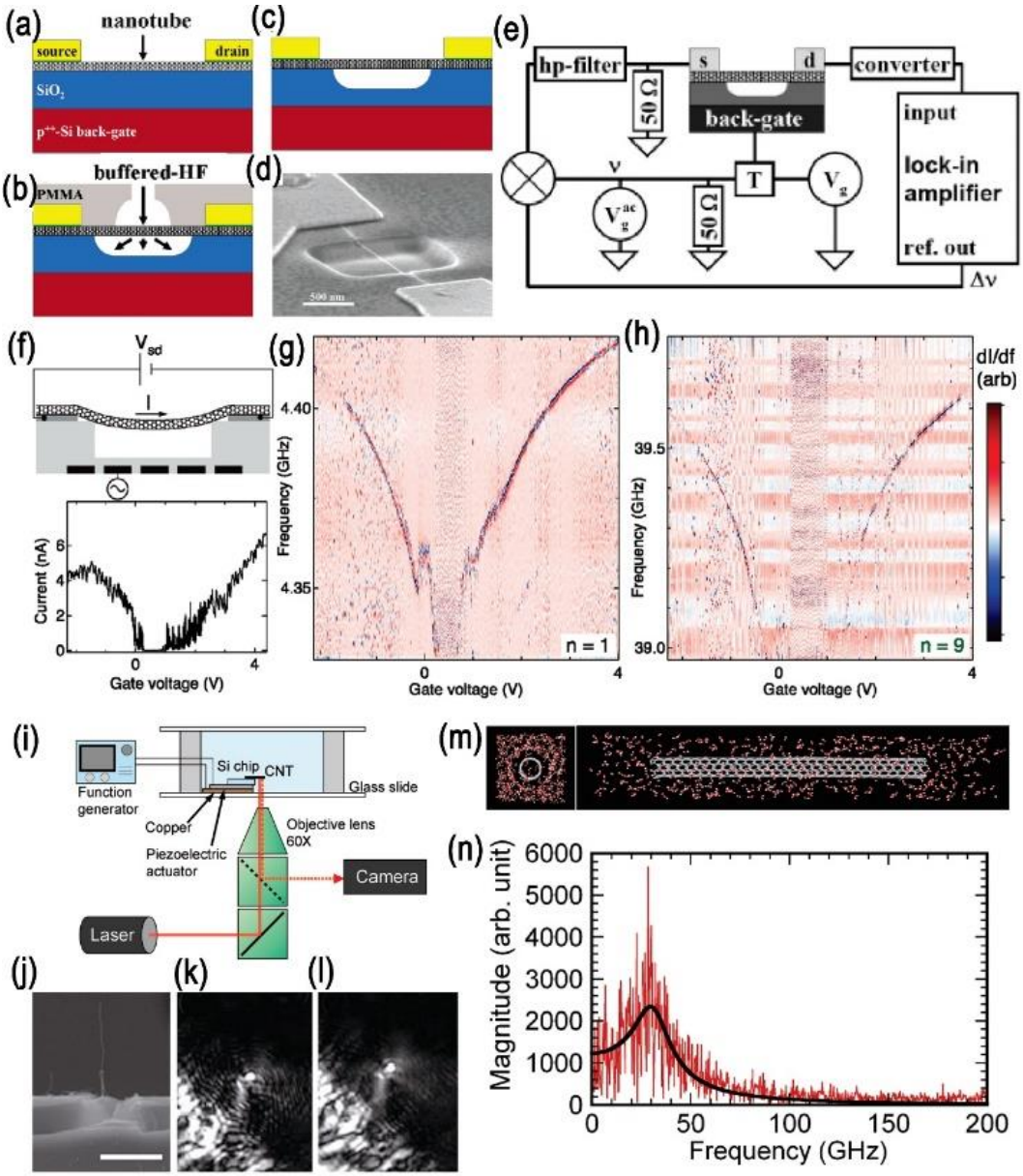

Figure S11. (a) Nanotube transistor morphology with a highly p-doped substrate as a back-gate, a SiO_2 layer, and a CVD-grown SWCNT clamped by Au/Cr electrodes. (b) Isotropic etching of the exposed SiO_2 layer with buffered HF in an etch mask defined in PMMA. (c) Suspended SWCNT resonator with its clamping points defined by the SiO_2 nanotube interfaces. (d) SEM image of a suspended nanotube fabricated with a PMMA etch mask. (e) Schematic overview of the measurement setup. (f) Top: schematic of the device and measurement circuit. Down: current through the device as

a function of dc voltage on all gates with V_{sd} = 2 mV. (g, h) Numerically differentiated dI/df as a function of gate voltage and microwave frequency for the fundamental (g) and ninth (h) modes. (i) Homemade inverted optical microscope to detect the vibration of CNT cantilevers. (j) Representative scanning electron and (k, l) optical micrographs of a CNT cantilever. Bar in (j) represents 10 μm. (m-n) Molecular dynamics simulation of the CNT vibration. (a-e) Reprinted with permission from ref 118. Copyright 2006 American Chemical Society. (f-h) Reprinted with permission from ref 121. Copyright 2011 American Chemical Society. (i-n) Reprinted with permission from ref 123. Copyright 2010 American Chemical Society.

3.5 Mass sensor

CNTs show a lot advantages as ultra-sensitive mass sensors due to their high Young's modulus. In 2008, Bockrath *et al.* reported that the doubly-clamped suspended CNTs could be used as an atomic-scale mass sensor.[114] The inertial atom mass and the CNT mass was determined by the shifts in the resonance frequency of the CNTs. Zettl *et al.* reported an atomic mass-scale nanomechanical mass sensor with a sensitivity of 1.3×10^{-25} kg $Hz^{-1/2}$ (or 0.40 gold atoms $Hz^{-1/2}$) at room temperature using a suspended CNT (Figure S12a-d).[115] Different from traditional mass sensors, this CNT-based mass sensor does not need the ionization of the testing sample and very sensitive to large molecules. In 2013, Bachtold *et al.* reported the fabrication of a mass sensor with a resolution of 1.7 yg using a 150 nm long CNT with vibration frequency of 2 GHz, which can even detect the adsorption of naphthalene molecules and the measurement of the binding energy of a xenon atom on the CNT surface (Figure S12e-i).[130] These

ultrasensitive CNT-based mass sensor have wide applications in numerous fields such as surface science, magnetometery and mass spectrometry, *etc*.

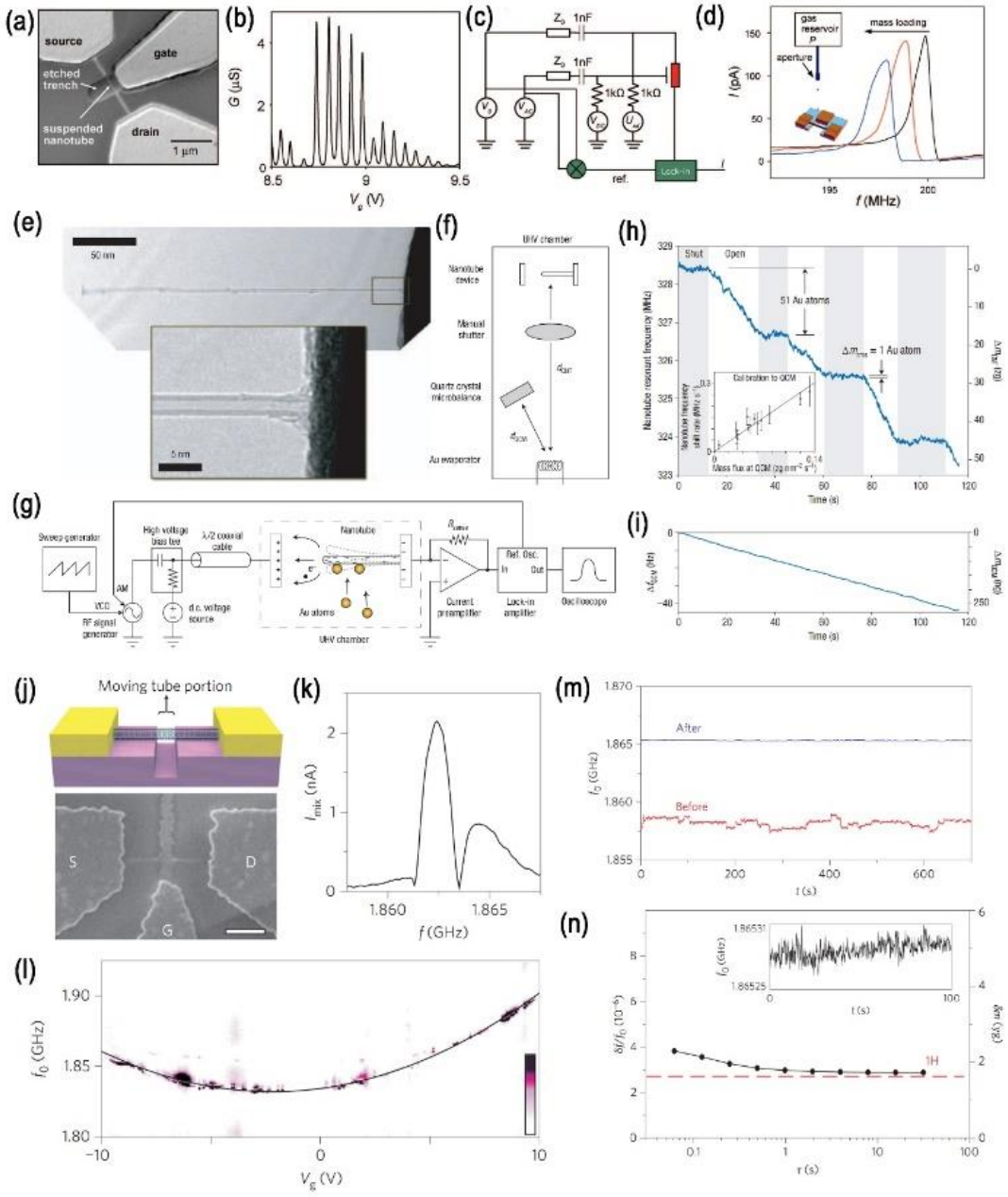

Figure S12. (a-c) Device morphology of suspended carbon nanotubes, single-electron transistor characteristics, and high-frequency measurement setup. (d) Response of nanomechanical resonance under mass loading and experimental setup. (e) TEM images of a nanomechanical mass spectrometer device constructed from a double-

walled carbon nanotube. (f) Physical layout of the entire nanomechanical mass spectrometer apparatus. (g) Schematic of the mechanical resonance detection circuit. (h) The nanotube's resonant frequency (left y-axis) and change in adsorbed mass (right y-axis) versus time during evaporation of gold. (i) At the same time the QCM records a constant evaporation rate as demonstrated by the constant slope of the frequency shift (left y-axis) and change in mass (right y-axis). (j-k) Schematic (j) and scanning electron microscope image (k) of the device. Scale bar, 300 nm. (l) Mechanical resonance obtained by measuring the mixing current I_{mix} as a function of driving frequency f using the FM mixing technique at 6 K. (m) Resonance frequency f_0 as a function of the voltage applied on the side-gate electrode at 6 K. (n) Resonance frequency as a function of time at 6 K before and after current annealing. (a-i) Reprinted with permission from ref 115. Copyright 2008 Nature Publishing Group. (j-n) Reprinted with permission from ref 130. Copyright 2012 Nature Publishing Group.

3.6 Chemical sensor

In 2000, Dai *et al.* fabricated chemical sensors based on individual SWCNTs (Figure S13a-g).[131] It was found that there was a dramatic decrease or increase in the electrical resistance of a semiconducting SWCNTs when exposed to gaseous molecules such as NO_2 or NH_3, which served as the basis for CNT-based molecular chemical sensors with a fast response and a high sensitivity. Through the heating to high temperature or low recovery in ambient conditions, the sensor reversibility could be well obtained. In 2003, Chopra *et al.* fabricated a CNT-based gas sensor to detect the presence of many gases (for instance, NH_3, CO, N_2 , He, O_2 , and Ar) (Figure S13h-j).[132] In comparison with

other sensors, this sensor can detect gases with low concentrations with a short response time. This sensor showed high selectivity to different gases and could be used in a remote sensing devices. Li *et al.* reported the fabrication of a gas sensor for the detection of gas and organic vapor at room temperature using SWCNTs with a detection resolution of sub ppm to hundreds of ppm with detection limits of 262 ppb for nitrotoluene and 44 ppb for NO_2 in a linear response for concentrations for a time on the order of seconds.[133]

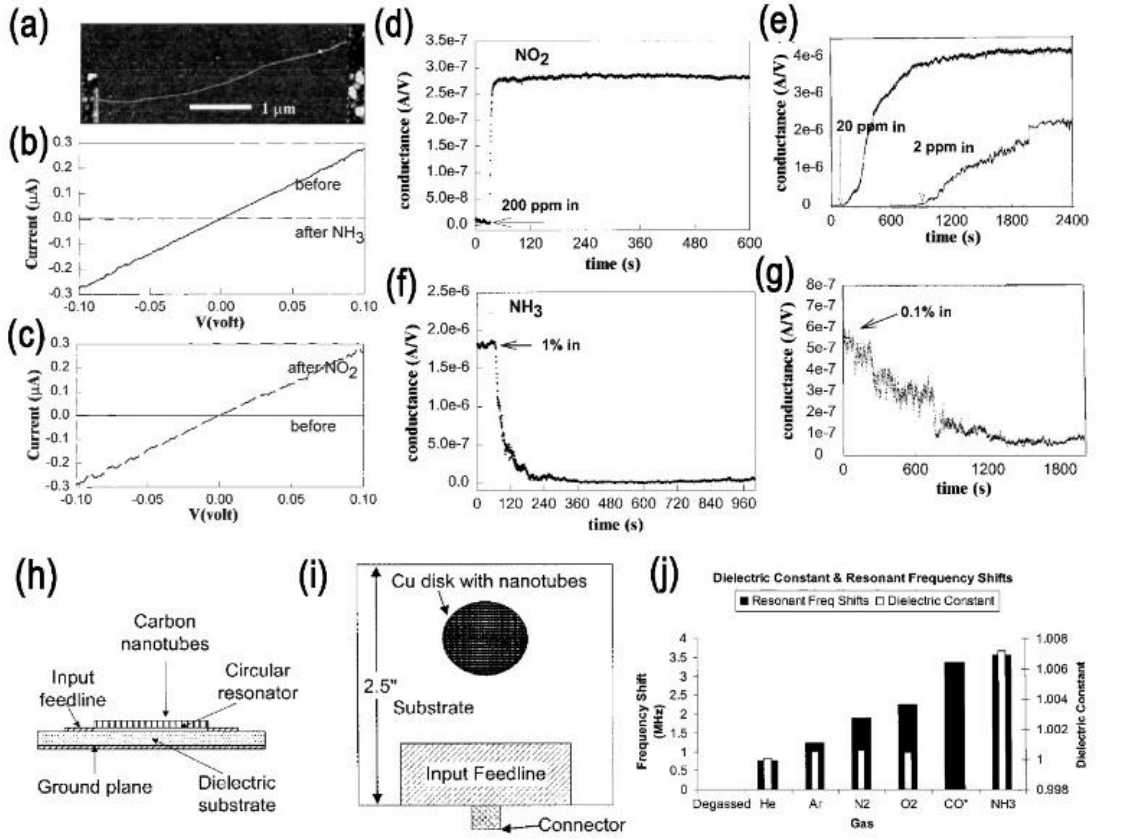

Figure S13. (a-c) Changes of electrical characteristics of a semiconducting SWCNT in chemical environments. (d) Conductance (under V_g = +4 V, in an initial insulating state) versus time in a 200-ppm NO_2 flow. (e) Data for a different semiconducting SWCNT sample in 20- and 2-ppm NO_2 flows. (f) Conductance (V_g = 0, in an initial conducting

state) versus time recorded with the same semiconducting SWCNT sample as in (A) in a flow of Ar containing 1% NH_3. (g) Data recorded with a different semiconducting SWCNT sample in a 0.1% NH_3 flow. (h) Schematic of front view of the resonator circuit. (i) Top view of the resonator sample coated with CNTs. (j) Resonant frequency shifts (solid bars) and dielectric constants (open bars) of various polar and nonpolar gases. (a-g) Reprinted with permission from ref 131. Copyright 2000 American Association for the Advancement of Science. (h-j) Reprinted with permission from ref 132. Copyright 2003 Elsevier.

3.7 Actuators

The ultralow friction between MWCNT shells makes the shells can rotate freely with respect to each other.[134-137] This superlubricious behavior of CNT shells renders them a promising candidate for the smart NEMS devices such as rotators and actuators. Zettl *et al.* fabricated a NEMS type actuators incorporated with a rotatable metal plate and a MWCNT acting as the critical motion element (Figure S14).[138] The total size of the actuator was about 300 nm with all components integrated on a silicon chip. The operation position and rate of the rotor was precisely controlled by a low voltage. It was found that the rotor plate could repeatedly oscillated between positions 180° apart and rotations of 360° over a wide range of temperature, frequency, harsh chemical environment and high vacuum without any fatigue or wear. This MWCNT-based actuator has promising potentials to be used in a wide range of application, such as switching devices, high-sensitivity mirrors, electromagnetic radiation transmitters, microfluidics systems-based fluid motion detectors, *etc*.

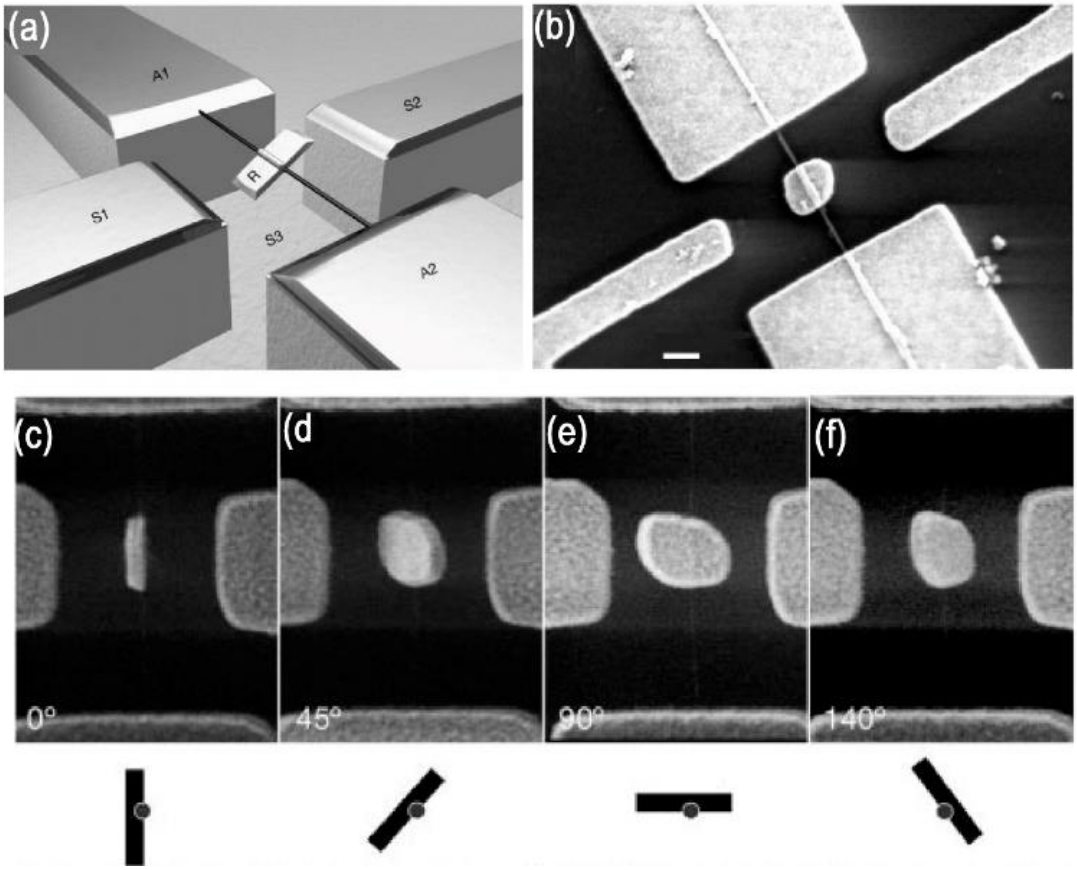

Figure S14. Integrated synthetic NEMS actuator. (a) Conceptual drawing of nanoactuator. (b) Scanning electron microscope (SEM) image of nanoactuator just prior to HF etching. Scale bar, 300 nm. (c-f) Series of SEM images showing the actuator rotor plate at different angular displacements. Scale bar, 300 nm. (a-f) Reprinted with permission from ref 138. Copyright 2003 Nature Publishing Group.

Supplementary References:

1. F. Ding, B. Kim and A. Rosen, *J. Phys. Chem. B*, 2004, **108**, 17369-17377.
2. Y. Shibuta and S. Maruyama, *Chem. Phys. Lett.*, 2003, **382**, 381-386.
3. J.-Y. Raty, F. Gygi and G. Galli, *Phys. Rev. Lett.*, 2005, **95**, 096103.
4. J. C. Burgos, H. Reyna, B. I. Yakobson and P. B. Balbuena, *J. Phys. Chem. C*, 2010, **114**, 6952-6958.
5. J. Gavillet, A. Loiseau, F. Ducastelle, S. Thair, P. Bernier, O. Stephan, J. Thibault and J.-C. Charlier, *Carbon*, 2002, **40**, 1649-1663.

6. Y. Ohta, Y. Okamoto, A. J. Page, S. Irle and K. Morokuma, *ACS Nano*, 2009, **3**, 3413-3420.
7. Y. Ohta, Y. Okamoto, S. Irle and K. Morokuma, *Carbon*, 2009, **47**, 1270-1275.
8. Y. Ohta, Y. Okamoto, S. Irle and K. Morokuma, *ACS Nano*, 2008, **2**, 1437-1444.
9. Q. Yuan, H. Hu and F. Ding, *Phys. Rev. Lett.*, 2011, **107**, 156101.
10. F. Ding, A. Rosen and K. Bolton, *J. Chem. Phys.*, 2004, **121**, 2775-2779.
11. D. Feng, K. Bolton and A. Rosen, *Comput. Mater. Sci.*, 2006, **35**.
12. D. Feng, B. Kim and A. Rosen, *J. Vac. Sci. Technol. A*, 2004, **22**.
13. J.-C. Charlier, A. De Vita, X. Blase and R. Car, *Science*, 1997, **275**, 647-649.
14. Y.-K. Kwon, Y. H. Lee, S.-G. Kim, P. Jund, D. Tománek and R. E. Smalley, *Phys. Rev. Lett.*, 1997, **79**, 2065.
15. S. Helveg, C. Lopez-Cartes, J. Sehested, P. L. Hansen, B. S. Clausen, J. R. Rostrup-Nielsen, F. Abild-Pedersen and J. K. Nørskov, *Nature*, 2004, **427**, 426-429.
16. Y. Li, W. Kim, Y. Zhang, M. Rolandi, D. Wang and H. Dai, *J. Phys. Chem. B*, 2001, **105**, 11424-11431.
17. H. Zhu, K. Suenaga, A. Hashimoto, K. Urita, K. Hata and S. Iijima, *Small*, 2005, **1**, 1180-1183.
18. A. J. Page, S. Minami, Y. Ohta, S. Irle and K. Morokuma, *Carbon*, 2010, **48**, 3014-3026.
19. P. Larsson, J. A. Larsson, R. Ahuja, D. Feng, B. I. Yakobson, D. Haiming, A. Rosen and B. Kim, *Phys. Rev. B*, 2007, **75**.
20. F. Ding, P. Larsson, J. A. Larsson, R. Ahuja, H. Duan, A. Rosén and K. Bolton, *Nano Lett.*, 2008, **8**, 463-468.
21. F. Ding and K. Bolton, *Nanotechnology*, 2006, **17**.
22. R. Xiang, B. Hou, E. Einarsson, P. Zhao, S. Harish, K. Morimoto, Y. Miyauchi, S. Chiashi, Z. Tang and S. Maruyama, *ACS Nano*, 2013, **7**, 3095-3103.
23. B. I. Yakobson, A. R. Harutyunyan and D. Feng, *PNAS*, 2009, **106**, 2506-2509.
24. S. M. Bachilo, M. S. Strano, C. Kittrell, R. H. Hauge, R. E. Smalley and R. B. Weisman, *Science*, 2002, **298**, 2361-2366.
25. S. M. Bachilo, L. Balzano, J. E. Herrera, F. Pompeo, D. E. Resasco and R. B. Weisman, *J. Am. Chem. Soc.*, 2003, **125**, 11186-11187.
26. Y. Miyauchi, S. Chiashi, Y. Murakami, Y. Hayashida and S. Maruyama, *Chem. Phys. Lett.*, 2004, **387**, 198-203.
27. K. Hirahara, M. Kociak, S. Bandow, T. Nakahira, K. Itoh, Y. Saito and S. Iijima, *Phys. Rev. B*, 2006, **73**, 195420.
28. R. Rao, D. Liptak, T. Cherukuri, B. I. Yakobson and B. Maruyama, *Nat. Mater.*, 2012, **11**, 213-216.
29. M. Marchand, C. Journet, D. Guillot, J.-M. Benoit, B. I. Yakobson and S. T. Purcell, *Nano Lett.*, 2009, **9**, 2961-2966.
30. Q. Wen, W. Qian, J. Nie, A. Cao, G. Ning, Y. Wang, L. Hu, Q. Zhang, J. Huang and F. Wei, *Adv. Mater.*, 2010, **22**, 1867-1871.
31. F. Ding, Z. Xu, B. I. Yakobson, R. J. Young, I. A. Kinloch, S. Cui, L. Deng, P. Puech and M. Monthioux, *Phys. Rev. B*, 2010, **82**.
32. Y. Zhao, B. I. Yakobson and R. E. Smalley, *Phys. Rev. Lett.*, 2002, **88**, 185501.

33. S. Han, M. Yoon, S. Berber, N. Park, E. Osawa, J. Ihm and D. Tománek, *Phys. Rev. B*, 2004, **70**, 113402.
34. I.-H. Lee, S. Jun, H. Kim, S. Y. Kim and Y. Lee, *Appl. Phys. Lett.*, 2006, **88**, 011913.
35. S. A. Morin, M. J. Bierman, J. Tong and S. Jin, *Science*, 2010, **328**, 476-480.
36. F. Abild-Pedersen, J. K. Nørskov, J. R. Rostrup-Nielsen, J. Sehested and S. Helveg, *Phys. Rev. B*, 2006, **73**, 115419.
37. S. Hofmann, G. Csanyi, A. Ferrari, M. Payne and J. Robertson, *Phys. Rev. Lett.*, 2005, **95**, 036101.
38. J. Robertson, S. Hofmann, M. Cantoro, A. Parvez, C. Ducati, G. Zhong, R. Sharma and C. Mattevi, *J. Nanosci. Nanotechnol.*, 2008, **8**, 6105-6111.
39. M. Ikeda, T. Yamasaki and C. Kaneta, *J. Phys.: Cond. Matter.*, 2010, **22**, 384214.
40. S. Nave and B. Jackson, *Phys. Rev. Lett.*, 2007, **98**, 173003.
41. F. Abild-Pedersen, O. Lytken, J. Engbæk, G. Nielsen, I. Chorkendorff and J. K. Nørskov, *Surf. Sci.*, 2005, **590**, 127-137.
42. D. Sorescu, *Phys. Rev. B*, 2006, **73**, 155420.
43. G. Hong, Y. Chen, P. Li and J. Zhang, *Carbon*, 2012, **50**, 2067-2082.
44. Y. Chen and J. Zhang, *Carbon*, 2011, **49**, 3316-3324.
45. B. Liu, D.-M. Tang, C. Sun, C. Liu, W. Ren, F. Li, W.-J. Yu, L.-C. Yin, L. Zhang and C. Jiang, *J. Am. Chem. Soc.*, 2010, **133**, 197-199.
46. Y. Homma, H. Liu, D. Takagi and Y. Kobayashi, *Nano Res.*, 2009, **2**, 793-799.
47. H. Liu, D. Takagi, S. Chiashi and Y. Homma, *Carbon*, 2010, **48**, 114-122.
48. Q. Wang, M.-F. Ng, S.-W. Yang, Y. Yang and Y. Chen, *ACS Nano*, 2010, **4**, 939-946.
49. V. Derycke, R. Martel, M. Radosavljevic, F. Ross and P. Avouris, *Nano Lett.*, 2002, **2**, 1043-1046.
50. B. Liu, W. Ren, C. Liu, C.-H. Sun, L. Gao, S. Li, C. Jiang and H.-M. Cheng, *ACS Nano*, 2009, **3**, 3421-3430.
51. B. L. Liu, W. Ren, L. Gao, S. Li, S. Pei, C. Liu, C. Jiang and H. M. Cheng, *J. Am. Chem. Soc.*, 2009, **131**, 2082-2083.
52. S. M. Huang, Q. Cai, J. Chen, Y. Qian and L. Zhang, *J. Am. Chem. Soc.*, 2009, **131**, 2094-2095.
53. L. Kang, Y. Hu, L. Liu, J. Wu, S. Zhang, Q. Zhao, F. Ding, Q. Li and J. Zhang, *Nano Lett.*, 2015, **15**, 403-409.
54. X. Yu, J. Zhang, W. Choi, J.-Y. Choi, J. M. Kim, L. Gan and Z. Liu, *Nano Lett.*, 2010, **10**, 3343-3349.
55. B. Liu, J. Liu, H.-B. Li, R. Bhola, E. A. Jackson, L. T. Scott, A. Page, S. Irle, K. Morokuma and C. Zhou, *Nano Lett.*, 2015, **15**, 586-595.
56. E. Gnecco, R. Bennewitz, T. Gyalog and E. Meyer, *J. Phys.: Cond. Matter.*, 2001, **13**, R619.
57. T. Fukuda, F. Arai and L. Dong, *Proc. IEEE*, 2003, **91**, 1803-1818.
58. M. Falvo, G. Clary, A. Helser, S. Paulson, R. Taylor, V. Chi, F. Brooks, S. Washburn and R. Superfine, *Microsc. Microanal.*, 1998, **4**, 504-512.
59. M. Falvo, G. Clary, R. Taylor, V. Chi, F. Brooks, S. Washburn and R. Superfine, *Nature*, 1997, **389**, 582-584.

60. P. Avouris, T. Hertel, R. Martel, T. Schmidt, H. Shea and R. Walkup, *Appl. Surf. Sci.*, 1999, **141**, 201-209.
61. H. Shea, R. Martel, T. Hertel, T. Schmidt and P. Avouris, *Microelec. Eng.*, 1999, **46**, 101-104.
62. T. Hertel, R. Martel and P. Avouris, *J. Phys. Chem. B*, 1998, **102**, 910-915.
63. M. Falvo, R. Taylor Ii, A. Helser, V. Chi, F. P. Brooks Jr, S. Washburn and R. Superfine, *Nature*, 1999, **397**, 236-238.
64. M.-F. Yu, T. Kowalewski and R. S. Ruoff, *Phys. Rev. Lett.*, 2000, **85**, 1456-1459.
65. J.-P. Salvetat, G. A. D. Briggs, J.-M. Bonard, R. R. Bacsa, A. J. Kulik, T. Stöckli, N. A. Burnham and L. Forró, *Phys. Rev. Lett.*, 1999, **82**, 944-947.
66. M. Nakajima, F. Arai and T. Fukuda, *Nanotechnology*, 2006, **5**, 243-248.
67. J. Cumings, P. G. Collins and A. Zettl, *Nature*, 2000, **406**, 586.
68. J. Huang, S. Chen, S. Jo, Z. Wang, D. Han, G. Chen, M. Dresselhaus and Z. Ren, *Phys. Rev. Lett.*, 2005, **94**, 236802.
69. M. Wang, L. M. Peng, J. Wang and Q. Chen, *Adv. Funct. Mater.*, 2006, **16**, 1462-1468.
70. M. Wang, J. Wang, Q. Chen and L. M. Peng, *Adv. Funct. Mater.*, 2005, **15**, 1825-1831.
71. X. L. Wei, Y. Liu, Q. Chen and L. M. Peng, *Nanotechnology*, 2008, **19**, 355304.
72. M. S. Wang, I. Kaplan-Ashiri, X. L. Wei, R. Rosentsveig, H. D. Wagner, R. Tenne and L. M. Peng, *Nano Res.*, 2008, **1**, 22-31.
73. X. Bai, D. Golberg, Y. Bando, C. Zhi, C. Tang, M. Mitome and K. Kurashima, *Nano Lett.*, 2007, **7**, 632-637.
74. M.-S. Wang, Q. Chen and L. M. Peng, *Adv. Mater.*, 2008, **20**, 724-728.
75. X. Wei, Q. Chen, Y. Liu and L. Peng, *Nanotechnology*, 2007, **18**, 185503.
76. M. Yu, M. J. Dyer, G. D. Skidmore, H. W. Rohrs, X. Lu, K. D. Ausman, J. R. Von Ehr and R. S. Ruoff, *Nanotechnology*, 1999, **10**, 244-252.
77. M.-F. Yu, O. Lourie, M. J. Dyer, K. Moloni, T. F. Kelly and R. S. Ruoff, *Science*, 2000, **287**, 637-640.
78. M.-F. Yu, B. I. Yakobson and R. S. Ruoff, *J. Phys. Chem. B*, 2000, **104**, 8764-8767.
79. L.-M. Peng, Q. Chen, X. Liang, S. Gao, J. Wang, S. Kleindiek and S. Tai, *Micron*, 2004, **35**, 495-502.
80. X. Wei, Q. Chen, L.-M. Peng, R. Cui and Y. Li, *J. Phys. Chem. C*, 2009, **113**, 17002-17005.
81. X. L. Wei, Y. Liu, Q. Chen, M. S. Wang and L. M. Peng, *Adv. Funct. Mater.*, 2008, **18**, 1555-1562.
82. X. Wei, Q. Chen, S. Xu, L. Peng and J. Zuo, *Adv. Funct. Mater.*, 2009, **19**, 1753-1758.
83. Q. Chen, S. Wang and L.-M. Peng, *Nanotechnology*, 2006, **17**, 1087.
84. X. Wei, Q. Chen, L. Peng, R. Cui and Y. Li, *Ultramicroscopy*, 2010, **110**, 182-189.
85. S. C. Lim, K. S. Kim, I. B. Lee, S. Y. Jeong, S. Cho, J.-E. Yoo and Y. H. Lee, *Micron*, 2005, **36**, 471-476.
86. J. Martínez, T. Yuzvinsky, A. Fennimore, A. Zettl, R. Garcia and C. Bustamante, *Nanotechnology*, 2005, **16**, 2493.
87. D. Zhang, J.-M. Breguet, R. Clavel, L. Philippe, I. Utke and J. Michler, *Nanotechnology*, 2009, **20**, 365706.
88. Y. Zhu and H. D. Espinosa, *Proc. Natl. Acad. Sci. USA*, 2005, **102**, 14503-14508.

89. B. Peng, M. Locascio, P. Zapol, S. Li, S. L. Mielke, G. C. Schatz and H. D. Espinosa, *Nat. Nanotechnol.*, 2008, **3**, 626-631.
90. J. U. Lee, P. Gipp and C. Heller, *Appl. Phys. Lett.*, 2004, **85**, 145.
91. J. U. Lee, *Appl. Phys. Lett.*, 2005, **87**, 73101-73101.
92. S. Wang, Z. Zhang, L. Ding, X. Liang, J. Shen, H. Xu, Q. Chen, R. Cul, Y. Li and L.-M. Peng, *Adv. Mater.*, 2008, **20**, 3258-+.
93. L. Jiao, X. Xian, B. Fan, Z. Wu, J. Zhang and Z. Liu, *J. Phys. Chem. C*, 2008, **112**, 7544-7546.
94. X. Ho, L. Ye, S. V. Rotkin, X. Xie, F. Du, S. Dunham, J. Zaumseil and J. A. Rogers, *Nano Res.*, 2010, **3**, 444-451.
95. S. Wang, Q. Zeng, L. Yang, Z. Zhang, Z. Wang, T. Pei, L. Ding, X. Liang, M. Gao, Y. Li and L.-M. Peng, *Nano Lett.*, 2011, **11**, 23-29.
96. L. Yang, S. Wang, Q. Zeng, Z. Zhang, Y. Li, W. Zhou, J. Liu and L.-M. Peng, *ACS Appl. Mater. Interfaces*, 2012, **4**, 1154-1157.
97. Q. Zeng, S. Wang, L. Yang, Z. Wang, Z. Zhang, L. Peng, W. Zhou and S. Xie, *Nano Res.*, 2012, **5**, 33-42.
98. A. D. Franklin, M. Luisier, S.-J. Han, G. Tulevski, C. M. Breslin, L. Gignac, M. S. Lundstrom and W. Haensch, *Nano Lett.*, 2012, **12**, 758-762.
99. N. M. Gabor, Z. Zhong, K. Bosnick, J. Park and P. L. McEuen, *Science*, 2009, **325**, 1367-1371.
100. H. Xu, S. Wang, Z. Zhang and L.-M. Peng, *Nano Lett.*, 2014, **14**, 5382-5389.
101. M. Fuhrer, B. Kim, T. Dürkop and T. Brintlinger, *Nano Lett.*, 2002, **2**, 755-759.
102. J. Cui, R. Sordan, M. Burghard and K. Kern, *Appl. Phys. Lett.*, 2002, **81**, 3260-3262.
103. T. Rueckes, K. Kim, E. Joselevich, G. Y. Tseng, C.-L. Cheung and C. M. Lieber, *Science*, 2000, **289**, 94-97.
104. W. Zhou, L. Ren, F. Lin, L. Jiao, T. Xue, X. Xian and Z. Liu, *Appl. Phys. Lett.*, 2008, **93**, 123115.
105. X. Liu, C. Lee, C. Zhou and J. Han, *Appl. Phys. Lett.*, 2001, **79**, 3329-3331.
106. Y. Hu, K. Yao, S. Wang, Z. Zhang, X. Liang, Q. Chen, L. Peng, Y. Yao, J. Zhang and W. Zhou, *Appl. Phys. Lett.*, 2007, **90**, 223116.
107. Z. Zhang, X. Liang, S. Wang, K. Yao, Y. Hu, Y. Zhu, Q. Chen, W. Zhou, Y. Li, Y. Yao, J. Zhang and L.-M. Peng, *Nano Lett.*, 2007, **7**, 3603-3607.
108. H. G. Craighead, *Science*, 2000, **290**, 1532-1535.
109. A. Naik, O. Buu, M. LaHaye, A. Armour, A. Clerk, M. Blencowe and K. Schwab, *Nature*, 2006, **443**, 193-196.
110. N. Flowers-Jacobs, D. Schmidt and K. Lehnert, *Phys. Rev. Lett.*, 2007, **98**, 096804.
111. X. Feng, C. White, A. Hajimiri and M. L. Roukes, *Nat. Nanotechnol.*, 2008, **3**, 342-346.
112. G. Zolfagharkhani, A. Gaidarzhy, S.-B. Shim, R. L. Badzey and P. Mohanty, *Phys. Rev. B*, 2005, **72**, 224101.
113. B. Lassagne, D. Garcia-Sanchez, A. Aguasca and A. Bachtold, *Nano Lett.*, 2008, **8**, 3735-3738.
114. H.-Y. Chiu, P. Hung, H. W. C. Postma and M. Bockrath, *Nano Lett.*, 2008, **8**, 4342-4346.

115. K. Jensen, K. Kim and A. Zettl, *Nat. Nanotechnol.*, 2008, **3**, 533-537.
116. K. C. Schwab and M. L. Roukes, *Phys. Today*, 2005, **58**, 36-42.
117. V. Sazonova, Y. Yaish, H. Üstünel, D. Roundy, T. A. Arias and P. L. McEuen, *Nature*, 2004, **431**, 284-287.
118. B. Witkamp, M. Poot and H. S. van der Zant, *Nano Lett.*, 2006, **6**, 2904-2908.
119. B. Witkamp, M. Poot, H. Pathangi, A. Hüttel and H. Van der Zant, *Appl. Phys. Lett.*, 2008, **93**, 111909.
120. H. Peng, C. Chang, S. Aloni, T. Yuzvinsky and A. Zettl, *Phys. Rev. Lett.*, 2006, **97**, 087203.
121. E. A. Laird, F. Pei, W. Tang, G. A. Steele and L. P. Kouwenhoven, *Nano Lett.*, 2011, **12**, 193-197.
122. A. K. Huttel, G. A. Steele, B. Witkamp, M. Poot, L. P. Kouwenhoven and H. S. van der Zant, *Nano Lett.*, 2009, **9**, 2547-2552.
123. S. Sawano, T. Arie and S. Akita, *Nano Lett.*, 2010, **10**, 3395-3398.
124. P. A. Greaney, G. Lani, G. Cicero and J. C. Grossman, *Nano Lett.*, 2009, **9**, 3699-3703.
125. Y. Liu, N. Wei, Q. Zeng, J. Han, H. Huang, D. Zhong, F. Wang, L. Ding, J. Xia, H. Xu, Z. Ma, S. Qiu, Q. Li, X. Liang, Z. Zhang, S. Wang and L.-M. Peng, *Adv. Opt. Mater.*, 2016, **4**, 238-245.
126. Y. Liu, N. Wei, Q. Zhao, D. Zhang, S. Wang and L.-M. Peng, *Nanoscale*, 2015, **7**, 6805-6812.
127. E. Cubukcu, F. Degirmenci, C. Kocabas, M. A. Zimmler, J. A. Rogers and F. Capasso, *Proc. Natl. Acad. Sci. USA*, 2009, **106**, 2495-2499.
128. L. Yang, S. Wang, Q. Zeng, Z. Zhang and L.-M. Peng, *Small*, 2013, **9**, 1225-1236.
129. N. Wei, Y. Liu, H. Xie, F. Wei, S. Wang and L.-M. Peng, *Appl. Phys. Lett.*, 2014, **105**.
130. J. Chaste, A. Eichler, J. Moser, G. Ceballos, R. Rurali and A. Bachtold, *Nat. Nanotechnol.*, 2012, **7**, 301-304.
131. J. Kong, N. R. Franklin, C. Zhou, M. G. Chapline, S. Peng, K. Cho and H. Dai, *Science*, 2000, **287**, 622-625.
132. S. Chopra, K. McGuire, N. Gothard, A. M. Rao and A. Pham, *Appl. Phys. Lett.*, 2003, **83**, 2280-2282.
133. J. Li, Y. Lu, Q. Ye, M. Cinke, J. Han and M. Meyyappan, *Nano Lett.*, 2003, **3**, 929-933.
134. J. Cumings and A. Zettl, *Science*, 2000, **289**, 602-604.
135. Y. Li, N. Hu, G. Yamamoto, Z. Wang, T. Hashida, H. Asanuma, C. Dong, T. Okabe, M. Arai and H. Fukunaga, *Carbon*, 2010, **48**, 2934-2940.
136. Z. Xia and W. Curtin, *Phys. Rev. B*, 2004, **69**, 233408.
137. Q. Zheng and Q. Jiang, *Phys. Rev. Lett.*, 2002, **88**, 45503.
138. A. Fennimore, T. Yuzvinsky, W. Q. Han, M. Fuhrer, J. Cumings and A. Zettl, *Nature*, 2003, **424**, 408-410.